

# The effect of normal stress on stacking fault energy in face-centered cubic metals

Yang Li and Yuri Mishin

Department of Physics and Astronomy, MSN 3F3,  
George Mason University, Fairfax, VA 22030, USA

January 12, 2026

## Abstract

Plastic deformation and fracture of FCC metals involve the formation of stable or unstable stacking faults (SFs) on (111) plane. Examples include dislocation cross-slip and dislocation nucleation at interfaces and near crack tips. The stress component normal to (111) plane can strongly affect the SF energy when the stress magnitude reaches several to tens of GPa. We conduct a series of DFT calculations of SF energies in six FCC metals: Al, Ni, Cu, Ag, Au, and Pt. The results show that normal compression significantly increases the stable and unstable SF energies in all six metals, while normal tension decreases them. The SF formation is accompanied by inelastic expansion in the normal direction. The DFT calculations are compared with predictions of several representative classical and machine-learning interatomic potentials. Many potentials fail to capture the correct stress effect on the SF energy, often predicting trends opposite to the DFT calculations. Possible ways to improve the ability of potentials to represent the stress effect on SF energy are discussed.

*Keywords:* FCC metals, stacking faults, DFT calculations, interatomic potentials

## 1 Introduction

A generalized stacking fault (GSF) is a planar defect created by sliding one part of a single crystal past another along a given atomic plane in a particular crystallographic direction [1]. The GSF energy (GSFE) describes the variation in potential energy per unit area as a function of the translation vector [2–5]. GSFE governs the dislocation behavior during plastic deformation and fracture of crystalline materials [1, 6]. It constitutes the critical input to the Peiers-Nabarro model [1, 7–11] and phase field dislocation dynamics simulations [12–14].

In face-centered cubic (FCC) metals, the most important GSF is obtained by sliding (111) atomic planes past each other in a  $\langle 211 \rangle$  direction. The GSFE has a local minimum at the translation  $\mathbf{u} = a[11\bar{2}]/6$ , where  $a$  is the cubic lattice constant. This minimum is separated from the perfect crystalline state ( $\mathbf{u} = 0$ ) by a local maximum. The metastable state corresponding to the energy minimum represents the intrinsic stacking fault (SF)

whose energy (SFE) is one of the most fundamental properties of FCC metals [1, 15]. The maximum corresponds to the unstable stacking fault (USF) whose energy (USFE) also plays an important role in many mechanical processes. For example, the SFE affects the dissociation width of full dislocations into Shockley partials. This width largely controls the dislocation cross-slip because the partials must recombine (thus eliminating the SF) before the dislocation can change the glide plane. The USFE controls the nucleation of dislocations at a crack tip [7, 16] and at surfaces and internal interfaces [17]. USFE is especially important in dislocation nucleation-controlled plasticity, which dominates the mechanical behavior of nanowires [18–20], pristine nanoparticles [21–23], and similar defect-free nanoscale objects.

GSFE can be altered by an applied stress [24, 25]. The most accurate investigations of the stress effect on GSFE utilize first-principles density functional theory (DFT) calculations. Brandl et al. [26] applied DFT calculations to study the GSFE in Al, Ni, and Cu under isotropic and shear strains. They found that under isotropic volume strain, the SFE of all three metals decreases with increasing volume, with Cu and Ni being less sensitive to the volume changes than Al. Under volume-conserving shear strain, the USFE of Ni and Al increases while the SFE decreases. In contrast, the GSFE curves for Cu exhibit only minor changes. Branicio et al. [27] computed the SFE in Cu under volumetric, uniaxial, and shear strains. It was found that under uniaxial strain applied along the [111] direction, the SFE of Cu increases as the strain changes from tension to compression. Andric et al. [28] analyzed the tensile stress dependence of the GSFE in Ni, Cu, Al, and Mg. Their DFT calculations have shown that in all three metals, the SFE decreases with increasing tensile stress normal to (111) planes.\*

Interatomic potentials have also been employed to study GSFEs under applied stresses. For example, calculations with an embedded-atom potential for Cu have shown that compressive (tensile) stress normal to the SF increases (decreases) the USFE and decreases (increases) the SFE [29]. The latter trend contradicts the DFT calculations [27, 28]. Similar results were obtained in a more recent study by Zhang et al. [30], who investigated the effect of stress on GSFE using embedded-atom potentials for Cu, Al, and Ni. When uniaxial stress ranging from  $-5$  GPa to  $5$  GPa was applied along the [111] direction, the USFE was found to increase as the stress changed from tension to compression. As will be shown later in this paper, this response is qualitatively consistent with DFT calculations. The SFE of Al also increased as the stress changed from tension to compression, which is also consistent with DFT calculations. However, the SFE in Cu and Ni decreased as the stress changed from tension to compression instead of increasing. Significant disagreements between potential predictions and DFT calculations for the stress effect on SFE were also reported by other authors [27, 28].

Such disagreements are highly alarming because the large-scale computer simulations of deformation and fracture of materials rely on interatomic potentials. The reliability of such simulations depends on the potential's ability to faithfully represent the impact of applied stresses on the GSFE and thus the dislocation behavior. This is especially important for the simulations of nano-mechanical processes involving high stresses on the level of tens of

---

\* Andric et al. [28] considered two different definitions of GSFE. The thermodynamically consistent definition of GSFE in the presence of applied stresses (see section 2.1 below) corresponds to what they called the GSF enthalpy.

GPa or higher, including shock deformation and the deformation and failure of nanowires and defect-free nanoparticles. There is a pressing need to understand the extent and origin of the mentioned disagreements and find ways to reduce them.

In this work, we perform a systematic DFT investigation of the effect of normal stress on GSFE in FCC metals, focusing on the energies of the stable and unstable faults (SFE and USFE). We additionally investigate the effect of normal stress on the shear modulus and Poisson's ratio of the metal. The reason for including the elastic properties is that the dislocation dissociation width is controlled by the balance between the elastic repulsion between the Shockley partials and the SF tension. Thus, predictions of the stress effect on the dissociation width require the knowledge of both factors.

The calculations are performed for six FCC metals representing simple metals (Al), noble metals (Cu, Ag, Au, and Pt), and transition metals (Ni). The DFT results are compared with a set of representative interatomic potentials for these metals. We include several types of classical (also known as traditional [31]) potentials and three types of machine-learning (ML) potentials [32]. Our goal is to evaluate the capabilities of interatomic potentials to predict the correct SF energies in FCC metals, as well as the dislocation dissociation width, under high-stress conditions. After a detailed comparison of the potential predictions with DFT calculations, we discuss possible approaches to improve the reliability of classical potentials for modeling high-stress deformation of FCC metals.

## 2 Computational Methodology

### 2.1 DFT calculations

Two types of models are commonly employed in the DFT calculations of SFEs: the tilted-cell method [33, 34] and the slab method [26]. In the tilted-cell method, a shear is applied to the lattice vectors in a direction parallel to the prescribed slip plane to generate a single stacking fault while preserving periodic boundary conditions. In the slab method, a crystal slab with two open surfaces is constructed, and the stacking fault is generated by rigidly shifting the upper half of the slab relative to the lower half. The slab thickness must be large enough to minimize the surface effects on the fault energy. To further remove surface contributions to the energy, the faulted slab energy is compared with that of a reference slab containing the same open surfaces but without the stacking fault. Due to the presence of open surfaces, the stress state of the cell cannot be controlled precisely. Therefore, in this study, we adopted the tilted-cell method, which inherently avoids the influence of free surfaces.

All DFT calculations were carried out with the Vienna *Ab initio* Simulation Package (VASP) [35, 36] using the projector-augmented-wave (PAW) method [37] and the Perdew–Burke–Ernzerhof (PBE) [38] generalized gradient approximation for exchange–correlation. The PAW datasets employed here were PAW\_PBE Al (04Jan2001), Cu (22Jun2005), Au (04Oct2007), Pt (04Feb2005), Ni (02Aug2007), and Ag (02Apr2005). (The release date is indicated in parentheses.) A plane-wave kinetic-energy cutoff of 500 eV was used. To calculate the GSFE, a periodic cell containing 24 atoms arranged in 12 (111) atomic layers was constructed (Fig. 1(a)). The cell was orthogonal with the following crystallographic orientations of the Cartesian axes:  $X \parallel [1\bar{1}0]$ ,  $Y \parallel [11\bar{2}]$ , and  $Z \parallel [111]$ . Brillouin-zone sampling

employed Monkhorst–Pack  $48 \times 26 \times 4$  meshes. For the calculations of the shear modulus and Poisson’s ratio, a simulation cell containing 6 atoms arranged in 3 (111) atomic layers was created, and the Brillouin-zone sampling employed Monkhorst–Pack  $64 \times 36 \times 26$  meshes. First-order Methfessel–Paxton smearing with the width of 0.20 eV was applied during the Brillouin-zone integration. The electronic self-consistency criterion was set to  $10^{-7}$  eV or  $10^{-8}$  eV, depending on the material. The ionic relaxation was considered converged when the maximum residual force fell below  $10^{-3}$  eV  $\text{\AA}^{-1}$  or  $10^{-4}$  eV  $\text{\AA}^{-1}$ , depending on the material. Calculations for Ni were spin-polarized with the initial magnetic moments of  $0.6 \mu_B$  per Ni atom. Other elements were treated as non-magnetic.

The GSFE was computed by the following steps.

1. The initial fault-free structure was optimized by a conjugate-gradient scheme until forces and stresses met the convergence criteria, leaving the principal stress components along  $X$ ,  $Y$ , and  $Z$  close to zero.
2. A stacking fault was created by deforming the cell shape to triclinic (i.e., tilting the axis  $Z$  toward  $Y$ ) with the  $YZ$  shear component of a chosen magnitude  $u$  while keeping the Cartesian coordinates of all atoms fixed (no remapping) (Fig. 1(b)). Periodic boundary conditions were maintained in all directions. As a result, a stacking fault formed at the boundary of the periodic simulation cell, with the fault plane normal to [111].
3. With the cell shape and size held fixed, the total energy was minimized by relaxing the atomic positions only along the [111] direction (with the lateral components fixed). The relaxation was performed using a conjugate gradient algorithm and was terminated once the maximum force on any atom fell below  $10^{-3}$  eV  $\text{\AA}^{-1}$  or  $10^{-4}$  eV  $\text{\AA}^{-1}$ , depending on the material. After the relaxation, the normal stress component  $\sigma_n$  (along the [111] direction) was generally nonzero because introducing a fault is usually accompanied by an inelastic change in the atomic density in the faulted layer, whereas the cell length  $L$  along [111] was constrained to remain fixed.
4. To eliminate the residual stress, the cell length  $L$  was varied in increments of 0.02%, repeating step 3 after each increment until the normal stress  $\sigma_n$  became negligible.
5. The GSFE at the targeted normal stress  $\sigma_n$  was calculated using the relaxed perfect (from step 1) and faulted (from step 4) cells as reference configurations. Both cells were subjected to incremental uniaxial strains along [111] in steps of  $\pm 0.02\%$ , with step 3 repeated after each increment until  $\sigma_n$  in *both* cells matched the target. The cross-sectional area  $A$  perpendicular to [111] was held fixed (no lateral strain).

The GSFE  $\gamma$  was computed from the formula

$$\gamma(u) = \frac{E(u) - E(u = 0)}{A} - [L(u) - L(u = 0)] \sigma_n. \quad (1)$$

Here,  $E(u = 0)$  and  $L(u = 0)$  represent the energy and length of the perfect cell under stress  $\sigma_n$ , while  $E(u)$  and  $L(u)$  are the respective quantities for the faulted cell under the *same* stress. The second term in the right-hand side of Eq. (1) represents the work (per unit area)

done on the system by the external load. This term is subtracted from the total energy change to obtain the work of the local forces causing the atomic rearrangements and bond distortions within the fault region during its creation. This is the proper thermodynamic definition of the interface/fault energy. Note that the lattice regions outside the SF are in the same physical state as in the reference perfect lattice system.

The procedure described above is time-consuming and computationally expensive in the DFT calculations. Therefore, we applied it only to obtain the intrinsic SFE ( $\gamma_{\text{SF}}$ ) corresponding to the displacement  $u = \frac{a}{6}[11\bar{2}]$ . For other shear displacements  $u$ , the GSFE was evaluated as

$$\gamma(u) = \frac{E_{L(u=0)}(u) - E(u=0)}{A}, \quad (2)$$

where  $E_{L(u=0)}(u)$  is the energy of the faulted cell that has the same length  $L(u=0)$  as the perfect cell. Eq. (2) calculates the energy difference between the perfect and faulted cells with the same length along the [111] direction. The normal stress in the perfect cell meets the target value of  $\sigma_n$ , whereas  $\sigma_n$  in the faulted cell does not exactly match the target value but remains close. In other words, Eq. (2) compares the energies of the perfect and faulted cells at fixed cell length, whereas Eq. (1) compares them at a fixed stress. Eq. (2) requires fewer DFT calculations because it bypasses the step of determining the faulted cell length corresponding to the target stress. We compared the SFE values predicted by Eqs. (1) and (2) and found that they differed by less than 3% over the entire stress range considered in this work, from  $-20$  to  $20$  GPa. Thus, to reduce computational cost, we used Eq. (2) to calculate the GSFE and USFE while still using the exact Eq. (1) for the SFE calculations. We note that Eq. (2) was frequently employed in previous DFT studies of GSFE [26, 27], in which the outermost layers of the faulted cell were held fixed during the shear displacement (i.e., under a fixed-strain or clamped-boundary condition).

For the shear modulus and Poisson's ratio calculations, the structural relaxation procedure was the same as in step 1 above. The cell length along [111] was varied incrementally, the structure was relaxed, and the normal stress  $\sigma_n$  was measured after each increment. This process was repeated until  $\sigma_n$  matched the target stress value. To compute the shear modulus,  $YZ$  shear strains  $\epsilon_{yz}$  ranging from  $-0.003$  to  $0.003$  were applied to the cell in increments of  $0.001$ . The corresponding shear stress  $\sigma_{yz}$  was measured as a function of  $\epsilon_{yz}$ . The measured stress-strain relation was fitted with a straight line, and its slope was taken as the shear modulus  $G$ . To compute Poisson's ratio, a set of small strains  $\epsilon_{xx}$ ,  $\epsilon_{yy}$ ,  $\epsilon_{zz}$ ,  $\epsilon_{xy}$ ,  $\epsilon_{yz}$ , and  $\epsilon_{zx}$  was applied sequentially, and the corresponding changes in stress were measured to obtain the components of the tangent stiffness tensor. The compliance tensor  $S_{ijkl}$  was then computed by inverting the stiffness tensor, and Poisson's ratio was calculated from the equation [39]

$$\nu_{ij} = -\frac{S_{iijj}}{S_{iiii}}. \quad (1)$$

This ratio represents the lateral strain in the  $j$ -th direction in response to axial strain applied in the  $i$ -th direction. In this work, we focused on the components  $\nu_{31}$  and  $\nu_{32}$  corresponding to the lateral strains in the  $X \parallel [1\bar{1}0]$  and  $Y \parallel [11\bar{2}]$  directions when tension or compression were applied in the  $Z \parallel [111]$  direction.

## 2.2 Calculations with interatomic potentials

Calculations with interatomic potentials were performed using the Large-scale Atomic/Molecular Massively Parallel Simulator (LAMMPS) [40]. For consistency, the simulation cells were similar in shape and size to those in the DFT calculations. The structures were relaxed by energy minimization until the changes in energy and force fell below  $etol = 10^{-10}$  and  $ftol = 10^{-10} \text{ eV } \text{\AA}^{-1}$ , respectively. In contrast to the DFT calculations, it was not necessary to repeatedly vary the supercell length in the [111] direction to achieve the target stress value. LAMMPS provides a direct functionality for controlling the stress along a specified direction. Consequently, all GSFE calculations were carried out using Eq. (1), without the need for the approximate Eq. (2). In the shear modulus calculations, shear strains  $\epsilon_{yz} = \pm 1.0 \times 10^{-6}$  were applied to a cell pre-deformed by a set normal stresses  $\sigma_n$ . The shear modulus was obtained from the relation  $G = \delta\sigma_{yz}/\delta\epsilon_{yz}$ , where  $\delta\sigma_{yz}$  is the difference in  $YZ$  stress between the two shear strains, and  $\delta\epsilon_{yz} = 2.0 \times 10^{-6}$  is the corresponding strain difference. Poisson's ratio was computed by the same method in the DFT calculations.

Table 1 lists the interatomic potentials for the six FCC metals tested in this work. Most of them are in the embedded-atom method (EAM) [41], modified EAM (MEAM) [42], and angular-dependent potential (ADP) [43] formats, which are most suitable for metallic systems. When we test more than one EAM potential for the same metal, we distinguish them by the first author's name.<sup>†</sup> For a broader exploration of the effect of the potential format on the results, we included modified Tersoff (MT) potentials for Pt [44] and Al (this work), which are conceptually distinct and lie well outside the EAM/MEAM/ADP domain. The MT formalism was initially developed for strongly covalent materials and was recently applied to construct interatomic potentials for Si [45, 46]. The potential includes only interactions with first neighbors and favors a particular angle between chemical bonds. However, if the cutoff range is extended well beyond the first coordination shell, an MT potential becomes a long-range many-body model explicitly capturing the bond-order effect. As such, it becomes similar in spirit to the EAM, MEAM, and ADP potentials despite having a different functional form. Long-range MT potentials can be equally successful in reproducing a wide range of properties of FCC metals, such as Al and Pt.<sup>‡</sup> For illustration, some of the properties predicted by the MT Al potential are summarized in the Supplementary Information file accompanying this article.

In addition to the classical potentials, we tested several ML potentials that are currently available for these metals, including a physically-informed neural network (PINN) potential for Al [47], a spectral neighbor analysis potential (SNAP) for Al [48], and moment tensor potentials (MTP) for Cu and Ag [49]. Since more classical and ML potentials are currently available for Al than for the other five metals studied here, we chose Al as a platform for the most detailed comparison of different potential models. To broaden this comparison, we developed a new MTP potential for Al. The DFT database used for training and the properties predicted by the MTP Al potential are presented in the Supplementary Information file. This enabled us to compare three ML potentials for Al in the PINN, SNAP, and MTP formats. Note that for Au and Pt, only classical interatomic potentials

---

<sup>†</sup>The first author's name is only used to label the potentials and does not imply any credit attribution.

<sup>‡</sup>An advantage of MT potentials for metals is that they can be crossed with MT potentials for covalent elements to describe mixed-bonding systems, such as Al-Si.

(EAM, ADP, MT) were tested since, to our knowledge, no suitable ML potentials are available for them. All potentials studied in this work are implemented in LAMMPS.

## 3 Results

### 3.1 DFT calculations

Fig. 2 shows the GSFE plots for the six metals under different normal stresses  $\sigma_n$ . The results were obtained by DFT calculations using Eq. (2). The curves are color-coded by the value of  $\sigma_n$ . We follow the stress sign convention adopted in LAMMPS, in which a compressive stress is considered positive and tensile stress is negative. The USFE values were determined from the first maximum of the GSFE curve, while the SFE values correspond to the local minimum. We also show the SFE energies calculated from Eq. (1) (without the fixed-cell length approximation), which are represented by the triangular markers. As mentioned above, the difference between the SFE values obtained from the two equations is small.

For all six metals, we applied the normal stresses ranging from  $-20$  GPa (tension) to  $20$  GPa (compression). All metals remain stable up to  $20$  GPa but some become mechanically unstable under large tensile stresses. Accordingly, the stress ranges considered in this work are as follows: Al ( $-10$  to  $20$  GPa), Cu ( $-20$  to  $20$  GPa), Au ( $-5$  to  $20$  GPa), Pt ( $-10$  to  $20$  GPa), Ni ( $-15$  to  $20$  GPa), and Ag ( $-10$  to  $20$  GPa).

The DFT results for the intrinsic SFE ( $\gamma_{SF}$ ), USFE, and the shear modulus are summarized in Figures 3 to 7. In addition to the raw results, we present normalized plots in which the fault energies and the elastic modulus are normalized by their stress-free values. All three properties (SFE, USFE, and  $G$ ) increase monotonically with the normal stress. Thus, normal compression increases the fault energies and simultaneously makes the metal stiffer, whereas normal tension produces the opposite effect. For Al, Cu, and Ni, these trends agree with previous DFT calculations by Andric et al. [28].<sup>§</sup> Branicio et al. [27] reported similar DFT results for SFE in Cu under both tension and compression (see their Fig. 3a).

Note the intersections between some of the curves, which signify changes in the ranking of the six metals. For example, Al has a smaller SFE than Ni in the stress-free state and under tension (Fig. 3(a)). However, at a few GPa of compression, the SFE of Al exceeds that of Ni. Note also that under sufficiently high tension, Al becomes a low-SFE metal. Similarly, the SFE of Au is low in the stress-free state and under tension but increases and eventually exceeds the SFE of Cu under compression. In the normalized format (Fig. 3(b)), the SFE plots split into two groups. The plots for Ag and Au merge together into a straight line, whereas the plots for the remaining metals merge into a different curve.

In Fig. 4(a), we plot the USFE as a function of normal stress for the six metals. Pt and Ni exhibit the highest USFE, while Ag and Au exhibit the lowest. Other than this, the USFEs do not consistently follow any particular ranking among the six metals. Some of the plots cross each other as  $\sigma_n$  varies within the stress interval studied here. In normalized coordinates (Fig. 4(b)), the curves again split into two groups, with Ag and Au forming one group and the remaining metals the other. This time, however, the groups are closer

---

<sup>§</sup>Andric et al. [28] considered only tensile loads.

together and their plots are more linear. The correlation within each group is much tighter, suggesting a possible scaling relation between USFE and normal stress across FCC metals.

Fig. 5 shows the stress dependence of the SFE/USFE ratio. This ratio is slightly below unity for Pt and Al and relatively small for Au, Cu, and especially Ag. Note that for Ag and Au, the SFE/USFE ratio increases under compression, whereas for Cu, Al, Ni, and Pt it decreases.

The atomic density within the SF region is generally different from that in the perfect FCC lattice. As a result, the formation of an SF is generally accompanied by inelastic deformation along the [111] direction. This deformation is measured by the difference

$$\Delta L(\sigma_n) = L(\sigma_n) - L_0(\sigma_n) \quad (2)$$

between the cell dimensions along [111] with ( $L(\sigma_n)$ ) and without ( $L_0(\sigma_n)$ ) the SF under the same normal stress  $\sigma_n$ . Note that  $\Delta L$  coincides with the term in the square brackets in Eq. (1) when  $u = a/\sqrt{6}$ . Since the SF formation does not change the cross-sectional area of the cell,  $\Delta L$  can be interpreted as the formation volume of the SF per unit area. The DFT calculations indicate that  $\Delta L$  is positive for all six metals under all stresses studied in this work (Fig. 6). In all cases, the SF region has a lower atomic density than the perfect FCC lattice, leading to the expansion of the system during the SF formation. Andric et al. [28] arrived at the same conclusion for Cu under a tensile stress.

Fig. 6 shows that for Ni, Al, and Pt,  $\Delta L$  decreases with increasing stress. The derivative  $-d\Delta L/d\sigma_n$  is a measure of compressibility of the SF region, which for these three metals is positive. For the remaining three metals, the slopes of the plots are small and could not be reliably resolved due to the scatter of the points.

The shear modulus  $G$  is a fairly linear function of stress with a positive slope (Fig. 7(a)). The six metals follow the ranking Ni > Pt > Cu > Al > Ag > Au, except for the recrossing of the Cu and Pt plots under a tension of about  $-5$  GPa. The normalized plot (Fig. 7(b)) shows that these metals generally follow a linear scaling relation with only Pt displaying a marked deviation.

Fig. 8(a) presents the DFT results for Poisson's ratio of the six metals. As expected from symmetry, the two components  $\nu_{31}$  and  $\nu_{32}$  nearly coincide within a small margin ( $\nu_{31} = \nu_{32} \equiv \nu$ ). In all cases,  $\nu$  increases with the applied stress, a behavior which is similar to that of the shear modulus. The  $\nu$  values span a wide interval from slightly below 0.1 for Cu under strong tension to nearly 0.5 for Au under strong compression. No particular ranking is followed because the plots for individual metals cross each other. In the normalized format (Fig. 8(b)), the plots collapse into two groups: Al, Cu, Ag, and Ni form one group and Au and Pt form another.

### 3.2 Calculations with interatomic potentials

Figure 9 summarizes the results of SFE calculations using the interatomic potentials for six metals. The results are compared with DFT calculations.

We first examine the comparison for Al (Fig. 9(a)). At zero stress, the potentials reproduce the SFE in reasonable agreement with DFT calculations. The only exception is the ADP potential, which grossly underestimates the DFT value. Under a tensile stress, all potentials under-predict the DFT values by up to a factor of 2. Under compression, only

the MTP potential demonstrates good agreement with DFT. The PINN and MT potentials follow the correct trend but reach a spurious maximum and start decreasing when  $\sigma_n$  exceeds 10 GPa. The EAM potentials perform poorly. When the compression reaches a few GPa, they sharply deviate from the DFT points and develop a negative slope. As compression increases, the SFE predicted by the EAM potentials falls below the zero-stress value. At a compression of 15 to 20 GPa, the EAM potentials predict that Al becomes a low-SFE metal, which is opposite to the DFT predictions. The ADP potential correctly reproduces the positive slope of the curve but the SFE remains significantly below the DFT values.

For Cu (Fig. 9(b)), the MTP potential demonstrates excellent agreement with DFT, except under a tensile stress below  $-15$  GPa when the SF becomes unstable. The MEAM potential correctly predicts a positive slope of the plot but significantly overestimates the SFE at all stresses. In addition, with this potential, the SF loses stability at  $\sigma_n < -15$  GPa. The SNAP potential also predicts the correct positive slope but under-predicts the SFE at all stresses below 15 GPa. In addition, with the SNAP potential, the SF loses stability below  $-10$  GPa. The EAM potential performs worst under both tension and compression. Although it accurately predicts the SFE in the stress-free state, it drastically underestimates the SFE under tension, eventually driving it to zero at about  $-15$  GPa. Under compression, the EAM curve has a negative slope instead of a positive one, leading to the incorrect prediction that compressive stresses reduce the SFE of Cu. The latter deficiency of this potential was previously noted in [27].

None of the Ni potentials tested in this work gives satisfactory results (Fig. 9(e)). The EAM Mishin potential agrees well with DFT in the stress-free state and under stresses  $\pm 5$  GPa but develops significant downward deviations outside this interval, including the loss of stability below  $-15$  GPa. The EAM Foiles potential deviates strongly from DFT at all stresses. Both EAM potentials predict a spurious maximum of the SFE followed by a negative slope at larger compressions, incorrectly indicating that compression decreases the SFE.

For Pt (Fig. 9(d)), the ADP potential approximately follows the DFT calculations at stresses  $\pm 5$  GPa but strongly deviates from them outside this interval. Additionally, the ADP curve develops a negative slope at  $\sigma_n > 10$  GPa. The curve computed with the MT potential has a similar shape and strongly overestimates the DFT values under compression. Both EAM potentials tested here perform poorly by grossly underestimating the SFE at all stresses.

Ag and Au pose the greatest challenge to potentials (Figs. 9(c,f)). The MTP potential for Ag at least has a positive slope, but significantly underestimates the SFE under compression and predicts the loss of stability below  $-15$  GPa. The remaining potentials predict the wrong slope of the plot at *all* stresses. Furthermore, under a sufficiently strong compression, the SFE becomes zero instead of increasing with stress and eventually reaching 3 to 4 times the stress-free value.

We next consider the USFE calculations for the six metals (Fig. 10). For Al, the MTP and PINN potentials accurately reproduce the DFT calculations under compression but under-predict the USFE under tension (Fig. 10(a)). The MT and EAM Mishin potentials match the DFT value at zero stress but underestimate it under both tension and compression. However, the general trend is reproduced correctly. The ADP potential reproduces the correct slope of the plot but is otherwise significantly less accurate. The EAM Mendelev

potential shows the largest deviations from DFT and predicts a spurious maximum at about 10 GPa. Fig. 10(a) does not include an USFE value for the EAM Mendelev potential at 20 GPa because the SFE becomes negative at this stress. For Cu, both the MTP and EAM potentials are in excellent agreement with DFT calculations, whereas the MEAM and SNAP potentials overestimate and underestimate the DFT, respectively (Fig. 10(b)). However, all four potentials correctly reproduce the positive slope of the curve. For Ni, the potentials reproduce the correct increasing trend (Fig. 10(e)), with the EAM Foiles potential being least accurate at all stresses. For Pt (Fig. 10(d)), the ADP and MT potentials agree with the DFT calculations reasonably well, but the EAM potential displays strong deviations. The EAM O'Brien potential fails to reproduce the correct behavior even qualitatively. For Ag, the MTP potential performs very well, whereas the EAM potential strongly deviates from DFT under tension (Fig. 10(f)). Finally, all Au potentials perform poorly (Fig. 10(c)). While the ADP potential predicts the correct trend, the EAM potentials fail to reproduce the DFT results even qualitatively.

Fig. 12 compares the stress dependencies of the shear modulus  $G$  for the six metals obtained by DFT calculations and predicted by the potentials. Reasonable agreement is observed for the MEAM potential for Cu, the ADP potential for Pt, the SNAP potential for Ni, and the MTP potential for Ag. In all other cases, the agreement is poorer. In a few cases, the potentials predict an incorrect slope of the curve under tensile stresses. This includes the EAM Mishin potential for Al (Fig. 12(a)) and the EAM Grachola and ADP potentials for Au (Fig. 12(c)). In addition, the EAM O'Brien potential for Pt changes the slope of the curve to negative at about 10 GPa (Fig. 12(d)). Several potentials display discontinuous behavior of  $G$  as a function of stress.

Next, we compare Poisson's ratio  $\nu$  (average of  $\nu_{31}$  and  $\nu_{32}$ ) predicted by the potentials and by DFT calculations (Fig. 13). As with the shear modulus, the most accurate agreement is displayed by the MTP potentials for Al, Ag, and Cu (in the latter case, a discontinuity is observed under tension). Incorrect slopes are exhibited by the EAM Al and EAM O'Brien Pt potentials under tension, as well as the EAM Mendelev potential for Al, the EAM O'Brien potential for Pt, and both EAM potentials for Au under compression. In addition, the EAM Foiles potential for Ni undergoes a discontinuous drop at about 10 GPa of compression.

As mentioned above, the DFT calculations predict that the SF formation volume  $\Delta L$  is positive for all six metals. Some potentials correctly reproduce the positive sign of  $\Delta L$  while others predict a negative sign (Fig. 11). For Al, only the MTP potential yields  $\Delta L > 0$  at all stresses tested here (Fig. 11(a)). The MT and PINN potentials predict that  $\Delta L$  reaches zero at 10 GPa of compression and becomes negative (alreilt small in magnitude) under further compression. According to the EAM potentials,  $\Delta L$  changes sign under a smaller compression and becomes negative and large in magnitude as  $\sigma_n$  increases. As a result, the SF formation is accompanied by a large inelastic contraction instead of the small expansion predicted by DFT. For Cu (Fig. 11(b)), all potentials reproduce the DFT results well except for the EAM potential. The latter predicts negative  $\Delta L$  values already in the stress-free state and even under a tension up to a few GPa. Although the magnitude of the negative  $\Delta L$  remains small ( $< 2 \times 10^{-2} \text{ \AA}$ ), this is an obvious flaw of the potential. For Pt (Fig. 11(d)), the EAM Zhou potential performs well, while the MT and ADP potentials incorrectly predict negative  $\Delta L$  values when compression exceeds 10 GPa. The EAM O'Brien potential is the

least accurate. It predicts negative  $\Delta L$  values with or without applied stresses except under a strong tension when the sign finally reverses. For Ni (Fig. 11(e)), only the SNAP potential keeps the SF volume positive at all stresses, although the magnitude of  $\Delta L$  is inaccurate and the slope of the curve is positive. The EAM potentials reverse the sign of  $\Delta L$  under a compression of about 5 GPa. For Ag (Fig. 11(f)), only the MTP potential reproduces the correct sign of  $\Delta L$  at all stresses. The EAM potential incorrectly predicts negative  $\Delta L$  values at all stresses except under a tension of  $\sigma_n < -5$  GPa. Finally, for Au, all potentials tested here perform poorly. They predict negative  $\Delta L$  values even without applied stresses. The ADP potential predicts negative  $\Delta L$  at all stresses. The EAM potential reverses the sign to positive only under a strong compression or tension, but even then, the magnitude of  $\Delta L$  remains significantly below the DFT values.

## 4 Discussion

### 4.1 DFT calculations

The DFT calculations performed in this work indicate that tensile and compressive stresses  $\sigma_n$  applied normal to the (111) plane strongly impact the stable and unstable stacking fault energies in FCC metals. For all six FCC metals studied here, both SFE and USFE increase monotonically with applied stress. Normal tension ( $\sigma_n < 0$ ) reduces the SFE and USFE while normal compression ( $\sigma_n > 0$ ) increases them. The impact of the stress can be very significant, reaching a factor of four in some cases. In particular, strong enough tension can suppress the SFE of Cu, Ag, and Au to nearly zero, while strong compression increases the SFE of Pt to about 0.4 J/m<sup>2</sup> (Figures 3 and 4). When replotted in normalized coordinates, the SFE versus stress curves for the six metals nearly collapse into a single master curve, suggesting the existence of a scaling law. The USFE versus stress curves also follow a scaling relation. The nature of this scaling requires further investigation.

The DFT calculations show that the SF formation is accompanied by local inelastic expansion of the SF core region in the direction normal to the SF plane. In other words, the SF formation volume  $\Delta L$  (per unit area) is positive, at least for the six metals tested here. The magnitude of the expansion is small (around 0.02 Å) for Cu, Ag, and Ni and larger (e.g., 0.05 to 0.1 Å) for the remaining metals. For Ni, Al, and Pt,  $\Delta L$  decreases with increasing stress. In the remaining cases, the trend could not be ascertained because of the scatter of the points.

It has long been assumed, based on the local atomic packing, that the SFE in FCC metals correlates with the energy difference  $\Delta E = E_{\text{HCP}} - E_{\text{FCC}}$  between the HCP and FCC phases per unit area  $A$  on the (111) plane; namely [50],

$$\gamma_{\text{SF}} = 2\Delta E/A. \quad (3)$$

To test this hypothesis and determine whether this correlation persists under a normal stress, we first calculated  $\Delta E$  as a function of atomic volume (Fig. 14). We kept the atomic volumes of the two phases equal because the HCP-like layer within the SF structure is forced to coherency with the surrounding FCC lattice. This layer slightly expands in the normal direction, changing its atomic volume. However, as discussed above, this expansion is small and can be neglected for this comparison. The triangular symbols in Fig. 14(a) mark the

$\Delta E$  values corresponding to the equilibrium FCC volume. Note that normal tension (i.e., higher atomic volume) decreases the energy difference between the two structures while normal compression (i.e., lower atomic volume) increases it. For all six metals,  $\Delta E$  remains positive both at the equilibrium atomic volume and under the tested stresses.

Fig. 14(b) compares the SFEs obtained by the DFT calculations with predictions from Eq.(3) at the equilibrium atomic volume. The bisecting dashed line corresponds to perfect agreement. Although the data points display a strong positive correlation (Pearson's correlation factor 0.997), Eq.(3) over-predicts the SFE values for Pt, and to a lesser extent, for Al and Ni.

The DFT calculations have shown that the shear modulus  $G$  and Poisson's ratio  $\nu$  strongly depend on the applied normal stress. Both  $G$  and  $\nu$  decrease under tension and increase under compression. In the stress interval examined here, their variation can reach a factor of four. Similar to the SF energies, both  $G$  and  $\nu$  follow scaling relations across the six metals.

As noted in section 1, the stable and unstable SF energies play an important role in plastic deformation of FCC metals. In particular, the dissociation width of a full dislocation into Shockley partials plays a critical role in cross-slip and in dislocation nucleation at surfaces, grain boundaries, and other interfaces. The equilibrium dissociation width  $d$  is dictated by the force balance between the elastic repulsion of the partials and their attraction due to the excess energy of the SF ribbon. As demonstrated by our DFT calculations, a compressive stress applied normal to the SF simultaneously increases the shear modulus and the SFE, thereby increasing both the elastic repulsion of the partials and their capillary attraction. Respectively, a tensile stress decreases both forces. It is not obvious *a priori* which factor (elasticity or SFE) will dominate the stress response of the dissociation width.

To glean a tentative answer to this question, we use the following equation for the dissociation width of an edge dislocation [1]:

$$d = \frac{Gb_p^2}{8\pi\gamma_{\text{SF}}} \frac{2 + \nu}{1 - \nu}, \quad (4)$$

where  $b_p = a/\sqrt{6}$  is the magnitude of the Burgers vector of a Shockley partial dislocation. We emphasize that Eq.(4) relies on continuum, isotropic linear elasticity, whereas some of the metals considered here are elastically anisotropic. In addition, the dissociation width is in some cases comparable to the lattice constant  $a$ , making the continuum approximation questionable. Despite these approximations, Eq.(4) can be useful for examining trends across the metals and for comparing the DFT calculations with predictions from interatomic potentials (see below). As evident from Fig. 15(a), the dissociation width computed from Eq.(4) is a monotonically increasing function of the normal stress for all six metals. The rate of increase is moderate to small, but persists across the entire stress interval studied here. The increasing trend indicates that the applied stress has a stronger effect on the elastic repulsion between the partials than on their attraction due to the SFE. The relatively low rate of increase is explained by the partial compensation between the stress-induced changes in the repulsive and attractive forces. Repotting in normalized coordinates reveals a scaling relation followed by Al, Ni, Cu, and Pt, with Ag and Au splitting off into a separate group (Fig. 15(b)).

## 4.2 Comparison with interatomic potentials

The DFT calculations performed in this work were compared with predictions of several representative interatomic potentials for the six metals. In most cases, the potentials fail to reproduce the SF properties and elastic coefficients under strong tension and compression. In some cases, the agreement with DFT is reasonable under relatively small stresses (e.g.,  $|\sigma_n| < 1$  GPa) but rapidly deteriorates as  $|\sigma_n|$  increases. In many cases, the potential predictions are diametrically opposite to DFT calculations. For example, many potentials predict that compressive stresses reduce the SF energy, whereas the DFT calculations predict the opposite trend. Many potentials predict a negative SF formation volume under compression or even at zero stress, while according to the DFT calculations, the SF formation volume is positive under all tensile and compressive stresses tested in this work. The agreement with DFT is somewhat better for USFE and elastic properties ( $G$  and  $\nu$ ), but some potentials still predict incorrect trends.

The classical potentials for Ag and Au perform worst. The MTP potentials for Al, Cu, and Ag and the PINN potential for Al demonstrate the best predictive capabilities. Generally, ML potentials can be more reliable at predicting high-stress behaviors. Their training database usually contains highly deformed structures informing the potential of the correct behavior under high-stress conditions. In contrast, classical potentials are fitted predominantly to equilibrium or near-equilibrium properties and are not sufficiently exposed to extreme deformations. Even when they are, reproducing both equilibrium and high-stress behaviors with a relatively small number of free parameters could be challenging. The existing classical potentials are most suitable for simulations under relatively small stresses. Great care should be taken when using them in simulations involving stresses on the level of 10 GPa and higher. Improving the performance of classical potentials in high-stress simulations might be possible but would require developing more general functional forms with a larger number of free parameters.

One way to improve classical potentials is through a stricter control of the HCP-FCC energy difference  $\Delta E$  as a function of atomic volume. As discussed previously,  $\Delta E$  correlates positively with SFE (Fig. 14). It can be shown that this correlation persists under positive and negative normal stresses (Fig. S6). Thus, the ability of a potential to reproduce the correct  $\Delta E$  values and their volume dependence is a predictor of the potential's reliability in reproducing the stress effect on the SFE. The existing potentials struggle with reproducing the correct behavior of  $\Delta E$  under elastic deformations. As noted above, the DFT values of  $\Delta E$  remain positive over a wide range of atomic volumes around the equilibrium state for all six metals. Fig. 16 compares the  $\Delta E$  versus volume plots predicted by DFT and computed with the potentials. As in the DFT calculations, the HCP structure was constrained such that its in-plane atomic density matched that of the FCC structure. While the DFT plots exhibit a smooth monotonic decrease of  $\Delta E$  with atomic volume, the  $\Delta E$  values predicted by some of the classical potentials display non-monotonic behaviors and change the sign from positive to negative. The MTP and PINN potentials still do not reproduce the DFT curves accurately but yield the correct positive sign of  $\Delta E$  and its monotonic decrease with atomic volume. The MT potentials for Al and Pt and the MEAM potential for Cu also perform reasonably well. The classical potentials for Ag and Au display the poorest performance. The non-monotonic and oscillatory behavior appears to be a common feature of the classical potentials. Future research may help elucidate the origin of this behavior

and explore ways to suppress them.

### 4.3 Application to dislocation dissociation

We previously mentioned that, due to a compensation effect, the dislocation dissociation width  $d$  is less sensitive to the applied stress than the elastic coefficients and the SFE separately. This prediction was made using Eq.(4), which relies on several approximations. It was interesting to test this prediction by direct simulations of the dislocation dissociation. As the test material, we chose Cu described by the MTP and EAM potentials. The MTP Cu potential is fairly accurate and can be considered a proxy for DFT calculations. As shown in Fig. 17, the MTP potential accurately reproduces the DFT values of  $d$  in the stress-free state and at moderate stresses of  $\pm 10$  GPa. Deviations are observed under higher tension and especially under stronger compression. However, the predicted dissociation width (between 2.5 and 3 nm) is in the correct ballpark and displays the slow increase with stress in agreement with DFT calculations. The EAM potential slightly underestimates the DFT values at moderate stresses ( $\pm 10$  GPa) but grossly overestimates them at higher stresses.

To compare the above predictions with direct simulations, we constructed a rectangular FCC model with the dimensions of  $0.9 \times 122 \times 100$  nm<sup>3</sup>. The edges of the simulation block were oriented with  $X \parallel [211]$ ,  $Y \parallel [01\bar{1}]$ , and  $Z \parallel [\bar{1}11]$ . The boundary conditions were periodic in the  $X$  direction and fixed in the  $Y$  and  $Z$  directions. Using the `atomman` toolkit [51], an edge dislocation was created at the center of the simulation block with the dislocation line parallel to the  $X$  axis. The construction used the lattice parameter and elastic constants corresponding to the tested potential. Atoms within a 0.5-nm-thick surface layer were frozen while all other atoms remained dynamic. The system was subjected to energy minimization followed by a molecular dynamics (MD) simulation in the NVE ensemble and then another energy minimization. As a result, the dislocation dissociated into Shockley partials with the dissociation width corresponding to the zero-stress condition. To apply uniaxial stress, a separate simulation block was created with the same dimensions and number of atoms and with all-periodic boundary conditions. An NPT MD simulation was performed at 1 K and with the imposed stress of 20 GPa (compression) or  $-10$  GPa (tension) parallel to the  $Z$  axis while keeping the  $X$  and  $Y$  dimensions fixed. The measured uniaxial strain was applied to the system containing the dislocation. The strain resulted in approximately the same stress parallel to [111] as in the perfect-lattice system. The equilibration procedure described above was reapplied, resulting in a new dissociation width corresponding to the applied stress.

The simulations yielded dislocation dissociation widths under stresses of 20 GPa, 0 GPa, and  $-10$  GPa with the two interatomic potentials. The results are summarized in the Supplementary Table S8 and illustrated in Fig. 18. With the MTP potential, the observed  $d$  values decrease from 4.8 nm to 2.6 nm as the stress increases from  $-10$  GPa to 20 GPa. This is contrary to Eq.(4), which predicts a mild increase from approximately 2.5 nm to 3 nm. With the EAM potential, the observed  $d$  values also decrease from 4.7 nm to 3.6 nm as the stress changes from  $-10$  GPa to zero. This trend also contradicts Eq.(4) but is in reasonable agreement with the MTP potential. However, compression causes a drastic increase in the dissociation width, which reaches 10.7 nm at 20 GPa. This increase is

predicted by Eq.(4) (cf. Fig. 17) and is in stark contrast with the MTP calculations. The unrealistically wide dislocation dissociation is an artifact of the EAM potential and may lead to unphysical behaviors of dislocations during high-stress deformation.

## 5 Conclusions

DFT calculations performed in this work demonstrate that uniaxial tensile and compressive stresses applied normal to (111) plane in FCC metals have a strong impact on the energies of the intrinsic and unstable SFs. Both energies increase under compression and decrease under tension. Normal stress also shifts the metal’s shear modulus  $G$  and Poisson’s ratio  $\nu$  in the same direction as the SF energies. Both the SF energies and the elastic coefficients follow scaling relations across the six FCC metals tested in this work. The DFT calculations show that the SF formation is accompanied by inelastic expansion of the SF core region in the normal direction.

Stress-induced changes in SF energies can affect many dislocation-controlled processes in FCC metals, such as dislocation nucleation at surfaces and interfaces in nanoscale objects and at crack tips. The magnitude of the stress effect varies. For example, the dislocation nucleation barrier depends on the USFE. The latter strongly depends on the magnitude and sign of the stress component normal to the slip plane, especially when it reaches a 10 GPa level. On the other hand, the width of the dislocation dissociation into Shockley partials is less sensitive to the normal stress because the latter changes the elastic repulsion force and the capillary attraction force between the partials in the same direction.

Atomistic simulations of deformation and fracture require spatial and temporal scales beyond those accessible to DFT calculations, and therefore rely on interatomic potentials. To assess the ability of potentials to reproduce the stress effect on SF energies, we tested several representative classical and ML potentials for the six metals. In addition to potentials taken from the literature, we included several classical and ML potentials developed in this work. Most of the potentials tested here perform poorly under large stresses. ML potentials in the MTP and PINN formats demonstrate markedly better agreement with DFT calculations than the classical potentials. Many classical potentials perform well when the normal stress is relatively small (say, below 1 GPa) but display significant deviations from the DFT calculations under larger positive and negative stresses (e.g.,  $\pm 10$  GPa and higher). Under high-stress conditions, some classical potentials produce artifacts, such as decrease in SFE under strong compression and unrealistically wide dislocation dissociation.

Classical interatomic potentials remain the workhorse of large-scale atomistic simulations of the mechanical behavior of materials. Although less accurate than ML potentials, they are computationally faster and often display more stable behaviors. This work suggests that they should be carefully tested before use in simulations involving high-stress conditions, such as shock deformation and nucleation-controlled plasticity in defect-free nanowires and nanoparticles. The development of new classical potentials for FCC metals should include training on larger deformations and fitting to the stress dependence of the HCP-FCC energy difference, or fitting to the SFE and USFE directly under normal tension and compression.

## Acknowledgments

This research was supported by the U.S. Department of Energy, Office of Basic Energy Sciences, Division of Materials Sciences and Engineering, under Award # DE-SC0023102.

## References

- [1] P. M. Anderson, J. P. Hirth, J. Lothe, *Theory of dislocations*, Cambridge University Press, 2017.
- [2] J. A. Zimmerman, H. Gao, F. F. Abraham, Generalized stacking fault energies for embedded atom fcc metals, *Modelling and Simulation in Materials Science and Engineering* 8 (2000) 103.
- [3] G. Lu, N. Kioussis, V. V. Bulatov, E. Kaxiras, Generalized-stacking-fault energy surface and dislocation properties of aluminum, *Phys. Rev. B* 62 (2000) 3099–3108.
- [4] J. A. Yan, C. Y. Wang, S. Y. Wang, Generalized stacking fault energy and dislocation properties in bcc Fe: A first-principles study, *Phys. Rev. B* 70 (2004) 174105.
- [5] C. Wang, H. Wang, T. Huang, X. Xue, F. Que, Q. Jiang, Generalized-stacking-fault energy and twin-boundary energy of hexagonal close-packed Au: A first-principles calculation, *Scientific Reports* 5 (2015) 10213.
- [6] V. Bulatov, F. F. Abraham, L. Kubin, B. Devincre, S. Yip, Connecting atomistic and mesoscale simulations of crystal plasticity, *Nature* 391 (1998) 669–672.
- [7] J. R. Rice, Dislocation nucleation from a crack tip: an analysis based on the peierls concept, *J. Mech. Phys. Solids* 40 (1992) 239–271.
- [8] G. S. Liu, X. Cheng, J. Wang, K. G. Chen, Y. Shen, Improvement of nonlocal Peierls-Nabarro models, *Comp. Mater. Sci.* 131 (2017) 69–77.
- [9] G. Lu, N. Kioussis, V. V. Bulatov, E. Kaxiras, The Peierls-Nabarro model revisited, *Philos. Mag. Lett.* 80 (2000) 675–682.
- [10] G. Schoeck, The core structure of dislocations. Peierls model vs. atomic simulations in Pd, *Compu. Mater. Sci.* 21 (2001) 124–134.
- [11] G. Lu, The Peierls—Nabarro model of dislocations: A venerable theory and its current development, Springer Netherlands, Dordrecht, 2005, pp. 793–811.
- [12] I. Beyerlein, A. Hunter, Understanding dislocation mechanics at the mesoscale using phase field dislocation dynamics, *Philosophical Transactions of the Royal Society A: Mathematical, Physical and Engineering Sciences* 374 (2016) 20150166.
- [13] H. Kim, N. Mathew, D. J. Luscher, A. Hunter, Phase field dislocation dynamics (PFDD) modeling of non-Schmid behavior in BCC metals informed by atomistic simulations, *Journal of the Mechanics and Physics of Solids* 152 (2021) 104460.

- [14] A. Hunter, I. J. Beyerlein, T. C. Germann, M. Koslowski, Influence of the stacking fault energy surface on partial dislocations in fcc metals with a three-dimensional phase field dislocations dynamics model, *Physical Review B—Condensed Matter and Materials Physics* 84 (2011) 144108.
- [15] V. Borovikov, M. I. Mendelev, A. H. King, Effects of stable and unstable stacking fault energy on dislocation nucleation in nano-crystalline metals, *Modelling and Simulation in Materials Science and Engineering* 24 (2016) 085017.
- [16] P. M. Anderson, J. R. Rice, Dislocation emission from cracks in crystals or along crystal interfaces, *Scr Metall* 20 (1986) 1467–1472.
- [17] G. Xu, C. Zhang, Analysis of dislocation nucleation from a crystal surface based on the Peierls–Nabarro dislocation model, *Journal of the Mechanics and Physics of Solids* 51 (2003) 1371–1394.
- [18] R. Cao, C. Deng, The ultra-small strongest grain size in nanocrystalline Ni nanowires, *Scripta Mater.* 94 (2015) 9–12.
- [19] Q.-J. Li, B. Xu, S. Hara, J. Li, E. Ma, Sample-size-dependent surface dislocation nucleation in nanoscale crystals, *Acta Materialia* 145 (2018) 19–29.
- [20] D. Mordehai, O. David, R. Kositski, Nucleation-controlled plasticity of metallic nanowires and nanoparticles, *Advanced Materials* 30 (2018) 1706710.
- [21] J. Amodeo, K. Lizoul, Mechanical properties and dislocation nucleation in nanocrystals with blunt edges, *Materials & Design* 135 (2017) 223–231.
- [22] A. Sharma, J. Hickman, N. Gazit, E. Rabkin, Y. Mishin, Nickel nanoparticles set a new record of strength, *Nature Communications* 9 (2018) 4102.
- [23] Z. Liang, N. T. Magar, R. K. Koju, I. Chesser, J. Zimmerman, Y. Mishin, E. Rabkin, Ultimate compressive strength and severe plastic deformation of equilibrated single-crystalline copper nanoparticles, *Acta Materialia* 276 (2024) 120101.
- [24] J. Yan, Z. Zhang, H. Yu, K. Li, Q. Hu, J. Yang, Z. Zhang, Effects of pressure on the generalized stacking fault energy and twinning propensity of face-centered cubic metals, *Journal of Alloys and Compounds* 866 (2021) 158869.
- [25] A. Linda, P. K. Tripathi, S. Nagar, S. Bhowmick, Effect of pressure on stacking fault energy and deformation behavior of face-centered cubic metals, *Materialia* 26 (2022) 101598.
- [26] C. Brandl, P. Derlet, H. Van Swygenhoven, General-stacking-fault energies in highly strained metallic environments: Ab initio calculations, *Physical Review B—Condensed Matter and Materials Physics* 76 (2007) 054124.
- [27] P. Branicio, J. Zhang, D. Srolovitz, Effect of strain on the stacking fault energy of copper: a first-principles study, *Physical Review B—Condensed Matter and Materials Physics* 88 (2013) 064104.

- [28] P. Andric, B. Yin, W. Curtin, Stress-dependence of generalized stacking fault energies, *Journal of the Mechanics and Physics of Solids* 122 (2019) 262–279.
- [29] M. Tschopp, D. McDowell, Influence of single crystal orientation on homogeneous dislocation nucleation under uniaxial loading, *Journal of the Mechanics and Physics of Solids* 56 (2008) 1806–1830.
- [30] L. Zhang, L. Cheng, X. Zhao, L.-Q. Pei, Molecular dynamics simulation on generalized stacking fault energies of fcc metals under preloading stress, *Chinese Physics B* 24 (2015) 088106.
- [31] Y. Mishin, Machine-learning interatomic potentials for materials science, *Acta Mater.* 214 (2021) 116980.
- [32] Y.-W. Zhang, V. Sorkin, Z. H. Aitken, A. Politano, J. Behler, A. P. Thompson, T. W. Ko, S. P. Ong, O. Chalykh, D. Korogod, E. Podryabinkin, A. Shapeev, J. Li, Y. Mishin, Z. Pei, X. Liu, J. Kim, Y. Park, S. Hwang, S. Han, K. Sheriff, Y. Cao, R. Freitas, Roadmap for the development of machine learning-based interatomic potentials, *Modelling and Simulation in Materials Science and Engineering* 33 (2025) 023301.
- [33] M. Jhon, A. Glaeser, D. Chrzan, Computational study of stacking faults in sapphire using total energy methods, *Physical Review B—Condensed Matter and Materials Physics* 71 (2005) 214101.
- [34] S. Kibey, J. Liu, D. D. Johnson, H. Sehitoglu, Generalized planar fault energies and twinning in cu–al alloys, *Applied physics letters* 89 (2006).
- [35] G. Kresse, J. Furthmüller, Efficiency of ab-initio total energy calculations for metals and semiconductors using a plane-wave basis set, *Computational materials science* 6 (1996) 15–50.
- [36] G. Kresse, J. Furthmüller, Efficient iterative schemes for ab initio total-energy calculations using a plane-wave basis set, *Physical review B* 54 (1996) 11169.
- [37] P. E. Blöchl, Projector augmented-wave method, *Physical review B* 50 (1994) 17953.
- [38] J. P. Perdew, K. Burke, M. Ernzerhof, Generalized gradient approximation made simple, *Physical review letters* 77 (1996) 3865.
- [39] J. F. Nye, *Physical Properties of Crystals*, Clarendon Press, Oxford, 1985.
- [40] A. P. Thompson, H. M. Aktulga, R. Berger, D. S. Bolintineanu, W. M. Brown, P. S. Crozier, P. J. In't Veld, A. Kohlmeyer, S. G. Moore, T. D. Nguyen, et al., Lammps—a flexible simulation tool for particle-based materials modeling at the atomic, meso, and continuum scales, *Computer physics communications* 271 (2022) 108171.
- [41] M. S. Daw, S. M. Foiles, M. I. Baskes, The embedded-atom method: a review of theory and applications, *Materials Science Reports* 9 (1993) 251–310.

- [42] M. I. Baskes, Modified embedded-atom potentials for cubic metals and impurities, *Phys. Rev. B* 46 (1992) 2727–2742.
- [43] Y. Mishin, M. J. Mehl, D. A. Papaconstantopoulos, Phase stability in the Fe-Ni system: Investigation by first-principles calculations and atomistic simulations, *Acta Mater.* 53 (2005) 4029–4041.
- [44] R. K. Koju, Y. Li, Y. Mishin, Comparison of interatomic potentials for platinum, In preparation, 2005.
- [45] T. Kumagai, S. Izumi, S. Hara, S. Sakai, Development of bond-order potentials that can reproduce the elastic constants and melting point of silicon for classical molecular dynamics simulation, *Comp. Mater. Sci.* 39 (2007) 457–464.
- [46] G. P. Purja Pun, Y. Mishin, Optimized interatomic potential for silicon and its application to thermal stability of silicene, *Phys. Rev. B* 95 (2017) 224103.
- [47] G. P. Pun, V. Yamakov, J. Hickman, E. Glaessgen, Y. Mishin, Development of a general-purpose machine-learning interatomic potential for aluminum by the physically informed neural network method, *Physical Review Materials* 4 (2020) 113807.
- [48] X.-G. Li, C. Hu, C. Chen, Z. Deng, J. Luo, S. P. Ong, Quantum-accurate spectral neighbor analysis potential models for Ni-Mo binary alloys and fcc metals, *Physical Review B* 98 (2018) 094104.
- [49] M. S. Nitol, M. J. E. Iriarte, D. E. Dickel, S. J. Fensin, Evaluating moment tensor potential in Ag-Cu alloy: Accuracy, transferability, and phase diagram fidelity, arXiv preprint arXiv:2508.18129 (2025).
- [50] G. S. Fanourgakis, V. Pontikis, G. Zérah, Phase stability and intrinsic stacking faults in aluminum under pressure, *Physical Review B* 67 (2003) 094102.
- [51] L. M. Hale, Z. T. Trautt, C. A. Becker, Atomistic manipulation toolkit (atomman), National Institute of Standards and Technology, 2023.
- [52] Y. Mishin, M. J. Mehl, D. A. Papaconstantopoulos, A. F. Voter, J. D. Kress, Structural stability and lattice defects in copper: Ab initio, tight-binding, and embedded-atom calculations, *Physical Review B* 63 (2001) 224106.
- [53] M. Mendelev, M. Kramer, C. A. Becker, M. Asta, Analysis of semi-empirical interatomic potentials appropriate for simulation of crystalline and liquid Al and Cu, *Philosophical Magazine* 88 (2008) 1723–1750.
- [54] Y. Mishin, D. Farkas, M. Mehl, D. Papaconstantopoulos, Interatomic potentials for monoatomic metals from experimental data and ab initio calculations, *Physical Review B* 59 (1999) 3393.
- [55] S. Starikov, I. Gordeev, Y. Lysogorskiy, L. Kolotova, S. Makarov, Optimized interatomic potential for study of structure and phase transitions in Si-Au and Si-Al systems, *Computational Materials Science* 184 (2020) 109891.

[56] S. A. Etesami, E. Asadi, Molecular dynamics for near melting temperatures simulations of metals using modified embedded-atom method, *Journal of Physics and Chemistry of Solids* 112 (2018) 61–72.

[57] G. Grotola, S. P. Russo, I. K. Snook, On fitting a gold embedded atom method potential using the force matching method, *The Journal of chemical physics* 123 (2005).

[58] G. P. Purja Pun, Au\_GLJ10\_3.eam.alloy (unpublished), NIST Interatomic Potentials Repository, 2017–Purja-Pun-G-P–Au, 2017. URL: <https://www.ctcms.nist.gov/potentials/system/Au/>.

[59] X. W. Zhou, R. Johnson, H. N. Wadley, Misfit-energy-increasing dislocations in vapor-deposited CoFe/NiFe multilayers, *Physical Review B* 69 (2004) 144113.

[60] C. O’Brien, C. Barr, P. Price, K. Hattar, S. Foiles, Grain boundary phase transformations in PtAu and relevance to thermal stabilization of bulk nanocrystalline metals, *Journal of Materials Science* 53 (2018) 2911–2927.

[61] S. M. Foiles, J. Hoyt, Computation of grain boundary stiffness and mobility from boundary fluctuations, *Acta Materialia* 54 (2006) 3351–3357.

[62] Y. Mishin, Atomistic modeling of the  $\gamma$  and  $\gamma'$ -phases of the Ni-Al system, *Acta Materialia* 52 (2004) 1451–1467.

[63] Y. Zuo, C. Chen, X. Li, Z. Deng, Y. Chen, J. Behler, G. Csányi, A. V. Shapeev, A. P. Thompson, M. A. Wood, et al., Performance and cost assessment of machine learning interatomic potentials, *The Journal of Physical Chemistry A* 124 (2020) 731–745.

[64] P. Williams, Y. Mishin, J. Hamilton, An embedded-atom potential for the Cu-Ag system, *Modelling and Simulation in Materials Science and Engineering* 14 (2006) 817.

[65] A. V. Shapeev, Moment tensor potentials: A class of systematically improvable interatomic potentials, *Multiscale Modeling & Simulation* 14 (2016) 1153–1173.

[66] K. Gubaev, E. V. Podryabinkin, A. V. Shapeev, Machine learning of molecular properties: Locality and active learning, *The Journal of chemical physics* 148 (2018).

[67] L. Vocablo, et al., The ab initio melting curve of aluminium, *arXiv preprint cond-mat/0108460* (2001).

[68] M. De Jong, W. Chen, T. Angsten, A. Jain, R. Notestine, A. Gamst, M. Sluiter, C. Krishna Ande, S. Van Der Zwaag, J. J. Plata, et al., Charting the complete elastic properties of inorganic crystalline compounds, *Scientific data* 2 (2015) 1–13.

[69] R. Tran, Z. Xu, B. Radhakrishnan, D. Winston, W. Sun, K. A. Persson, S. P. Ong, Surface energies of elemental crystals, *Scientific data* 3 (2016) 1–13.

- [70] R. Qiu, H. Lu, B. Ao, L. Huang, T. Tang, P. Chen, Energetics of intrinsic point defects in aluminium via orbital-free density functional theory, *Philosophical Magazine* 97 (2017) 2164–2181.
- [71] H. Zhuang, M. Chen, E. A. Carter, Elastic and thermodynamic properties of complex mg-al intermetallic compounds via orbital-free density functional theory, *Physical Review Applied* 5 (2016) 064021.
- [72] M. Iyer, V. Gavini, T. M. Pollock, Energetics and nucleation of point defects in aluminum under extreme tensile hydrostatic stresses, *Physical Review B* 89 (2014) 014108.
- [73] T. Sjostrom, S. Crockett, S. Rudin, Multiphase aluminum equations of state via density functional theory, *Physical Review B* 94 (2016) 144101.
- [74] J. F. Devlin, Stacking fault energies of be, mg, al, cu, ag, and au, *Journal of Physics F: Metal Physics* 4 (1974) 1865.
- [75] S. Ogata, J. Li, S. Yip, Ideal pure shear strength of aluminum and copper, *Science* 298 (2002) 807–811.
- [76] M. Jahnátek, J. Hafner, M. Krajčí, Shear deformation, ideal strength, and stacking fault formation of fcc metals: A density-functional study of al and cu, *Physical Review B—Condensed Matter and Materials Physics* 79 (2009) 224103.
- [77] S. Kibey, J. Liu, D. Johnson, H. Sehitoglu, Predicting twinning stress in fcc metals: Linking twin-energy pathways to twin nucleation, *Acta materialia* 55 (2007) 6843–6851.
- [78] P. Desai, Thermodynamic properties of aluminum, *International journal of thermophysics* 8 (1987) 621–638.
- [79] N. V. Kozyrev, V. V. Gordeev, Thermodynamic properties and equation of state for solid and liquid aluminum, *Metals* 12 (2022) 1346.
- [80] B.-Y. Ning, L.-Y. Zhang, An ab initio study of structural phase transitions of crystalline aluminium under ultrahigh pressures based on ensemble theory, *Computational Materials Science* 218 (2023) 111960.
- [81] A. Dewaele, P. Loubeyre, M. Mezouar, Equations of state of six metals above 94 gpa, *Physical Review B—Condensed Matter and Materials Physics* 70 (2004) 094112.
- [82] Y. Akahama, M. Nishimura, K. Kinoshita, H. Kawamura, Y. Ohishi, Evidence of a fcc-hcp transition in aluminum at multimegabar pressure, *Physical review letters* 96 (2006) 045505.
- [83] R. t. Stedman, G. Nilsson, Dispersion relations for phonons in aluminum at 80 and 300 k, *Physical Review* 145 (1966) 492.
- [84] J. F. Ziegler, J. P. Biersack, The stopping and range of ions in matter, in: *Treatise on heavy-ion science: volume 6: astrophysics, chemistry, and condensed matter*, Springer, 1985, pp. 93–129.

- [85] A. Tago, I. Tonaka, First principles phonon calculations in materials science, *Scripta Mater.* 108 (2015) 1–5.
- [86] J. Morris, C. Wang, K. Ho, C. Chan, Melting line of aluminum from simulations of coexisting phases, *Phys. Rev. B* 49 (1994) 3109–3115.
- [87] J. Morris, X. Song, The melting lines of model systems calculated from coexistence simulations, *J. Chem. Phys.* 116 (2002) 9352–9358.
- [88] C. A. Howells, Y. Mishin, Angular-dependent interatomic potential for the binary Ni-Cr system, *Model. Simul. Mater. Sci. Eng.* 26 (2018) 085008.
- [89] J. Tersoff, New empirical approach for the structure and energy of covalent systems, *Phys. Rev. B* 37 (1988) 6991–7000.
- [90] J. Tersoff, Empirical interatomic potential for silicon with improved elastic properties, *Phys. Rev. B* 38 (1988) 9902–9905.
- [91] J. Tersoff, Modeling solid-state chemistry: Interatomic potentials for multicomponent systems, *Phys. Rev. B* 39 (1989) 5566–5568.

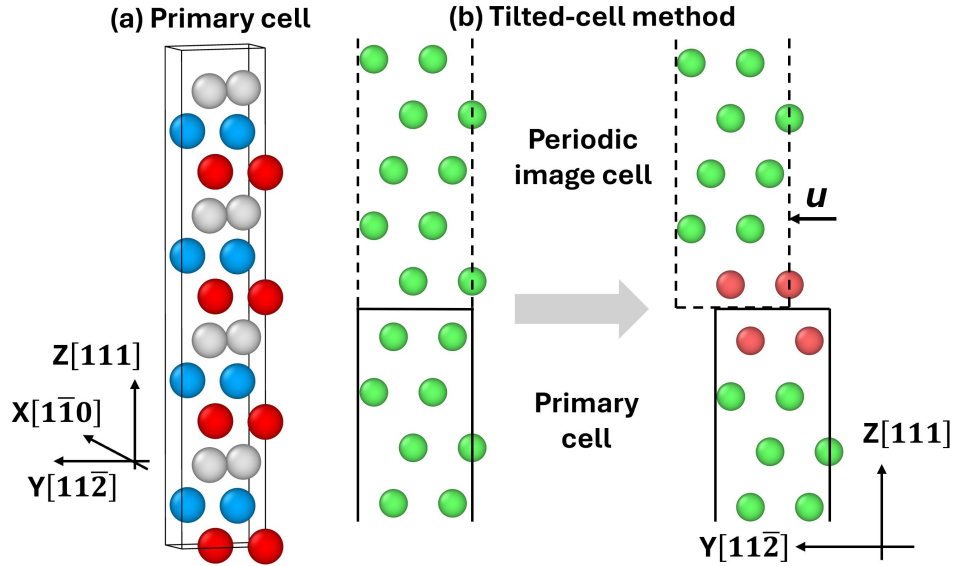


Figure 1: (a) Atomic structure of the cell used in the GSFE calculations. The cell contains 24 (111) layers, each with two atoms. The atoms are colored by their  $Z$  positions to provide better visualization of the structure. (b) Illustration of the tilted-cell method. By tilting the  $Z$  axis towards  $Y$  by an amount  $u$ , a stacking fault is created at the boundary between the primary cell and its periodic image. The solid rectangle marks the primary cell, and the dashed rectangle marks its periodic image. The atoms in FCC and non-FCC environments are shown in green and red, respectively.

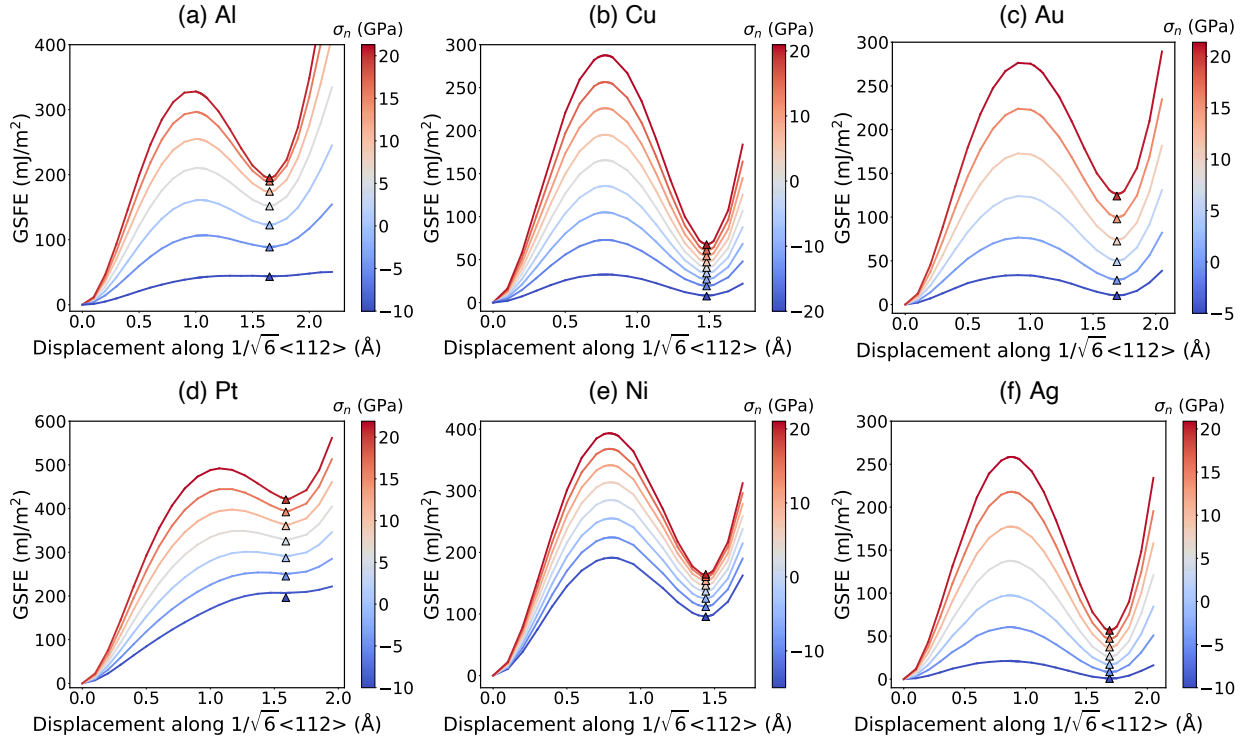


Figure 2: GSFE versus shear displacement under applied normal stress  $\sigma_n$  obtained by DFT calculations. (a) Al, (b) Cu, (c) Au, (d) Pt, (e) Ni, and (f) Ag. The curves were computed from Eq. (2). The triangular symbols represent SFE calculations from the exact Eq. (1).

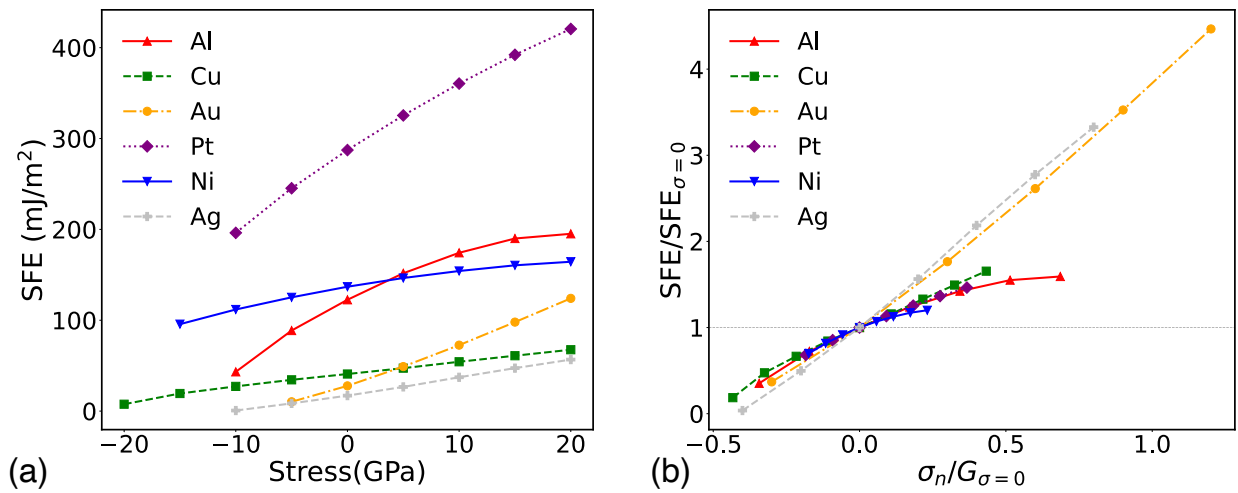


Figure 3: SFE in six FCC metals obtained by DFT calculations. (a) Physical coordinates. (b) Normalized coordinates.

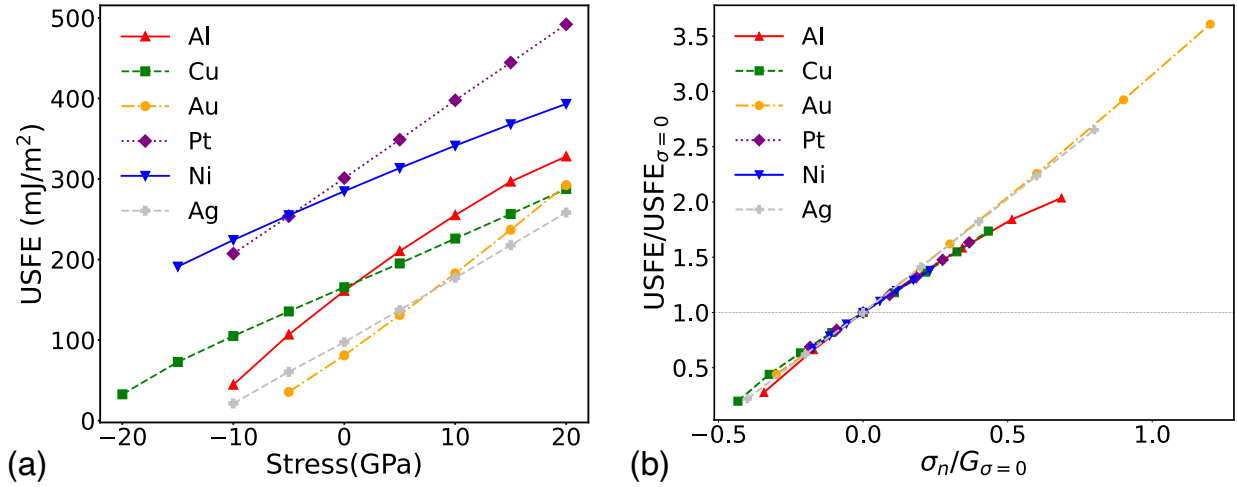


Figure 4: USFE in six FCC metals as a function of normal stress obtained by DFT calculations. (a) Physical coordinates. (b) Normalized coordinates.

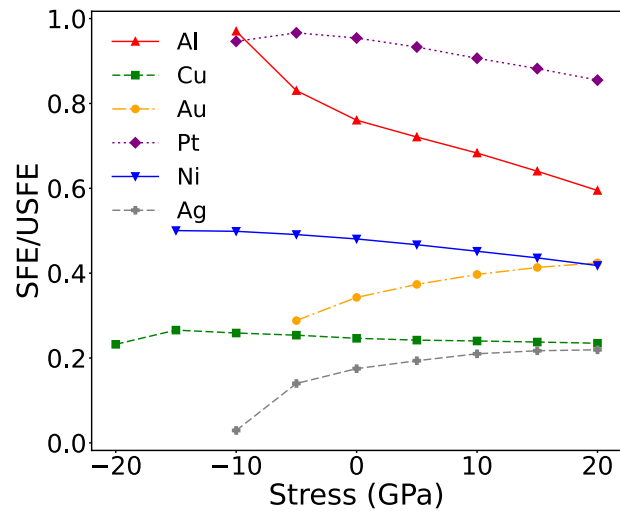


Figure 5: The ratio of the SFE and the USFE as a function of normal stress for six FCC metals obtained by DFT calculations.

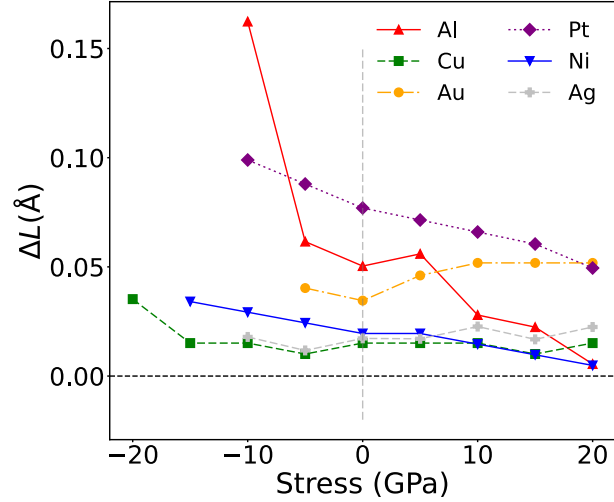


Figure 6: SF formation volume as a function of normal stress for six FCC metals obtained by DFT calculations.

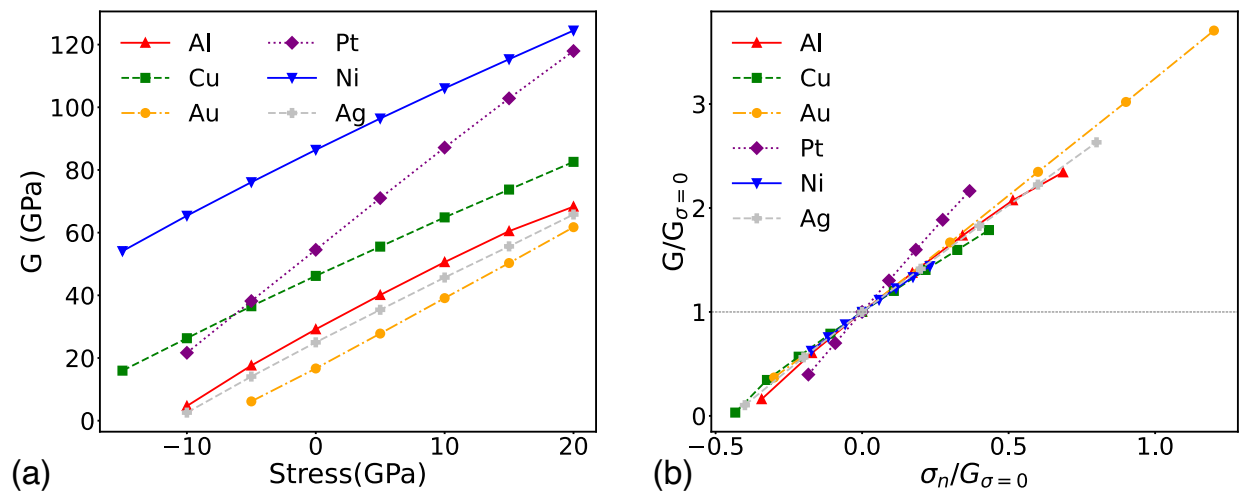


Figure 7: The shear modulus  $G$  as a function of normal stress for six FCC metals obtained by DFT calculations. (a) Physical coordinates. (b) Normalized coordinates.

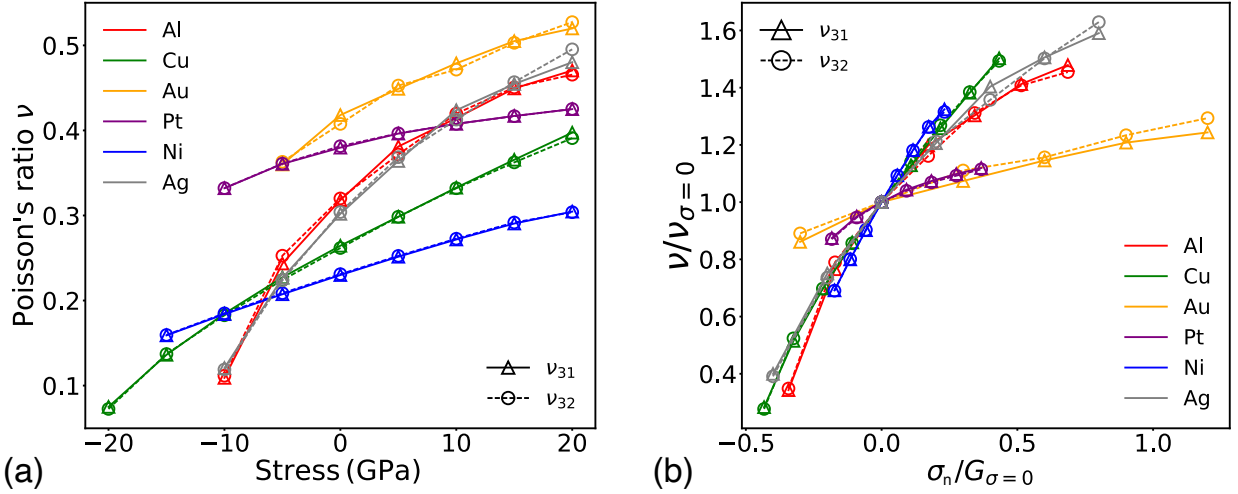


Figure 8: Poisson's ratios  $\nu_{31}$  and  $\nu_{32}$  as a function of normal stress for six FCC metals obtained by DFT calculations. (a) Physical coordinates. (b) Normalized coordinates.

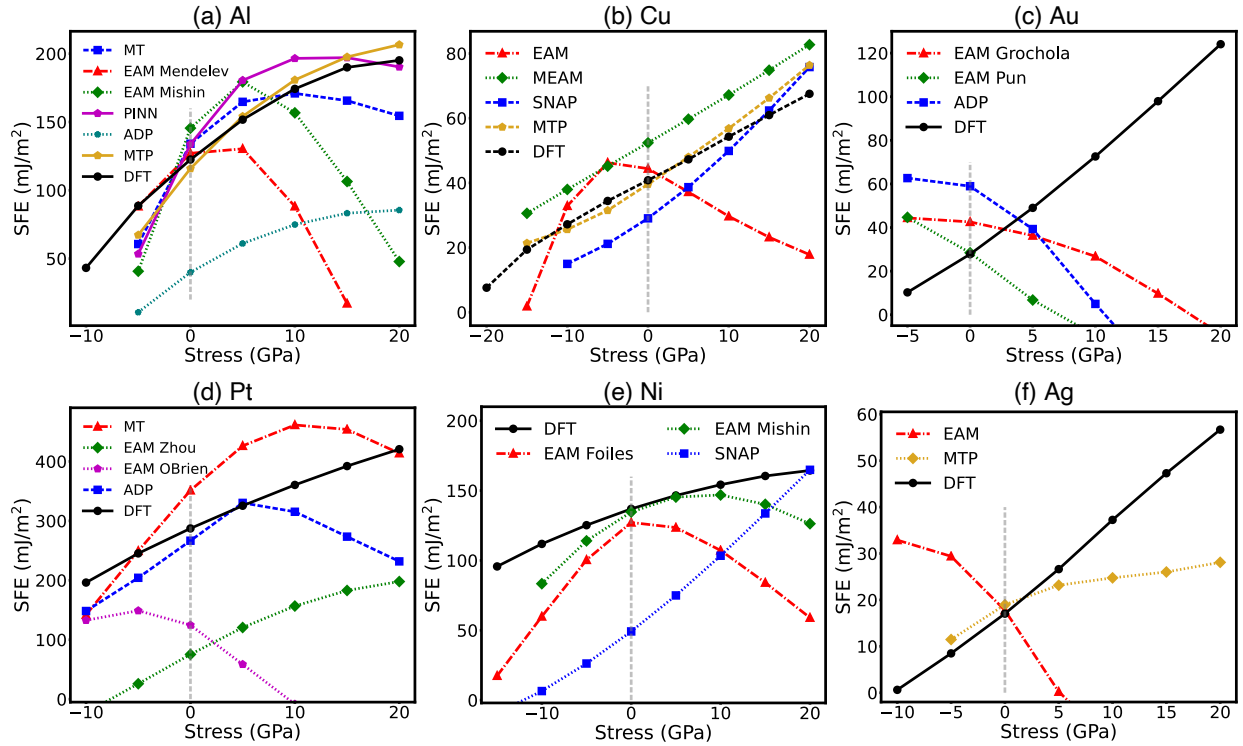


Figure 9: SFE versus applied normal stress obtained by DFT calculations and with interatomic potentials. (a) Al, (b) Cu, (c) Au, (d) Pt, (e) Ni, and (f) Ag. The vertical dashed line corresponds to zero stress and serves as a visual guide.

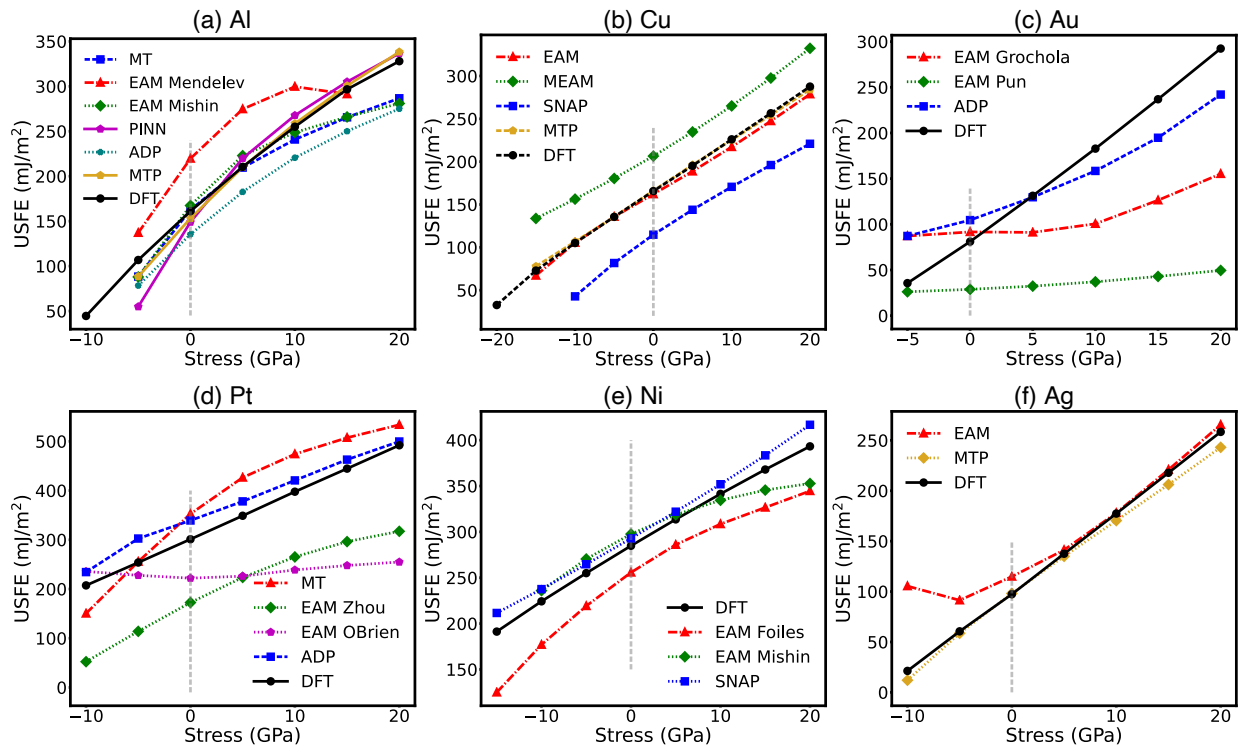


Figure 10: USFE versus applied normal stress obtained by DFT calculations and with interatomic potentials. (a) Al, (b) Cu, (c) Au, (d) Pt, (e) Ni, and (f) Ag. The vertical dashed line corresponds to zero stress and serves as a visual guide.

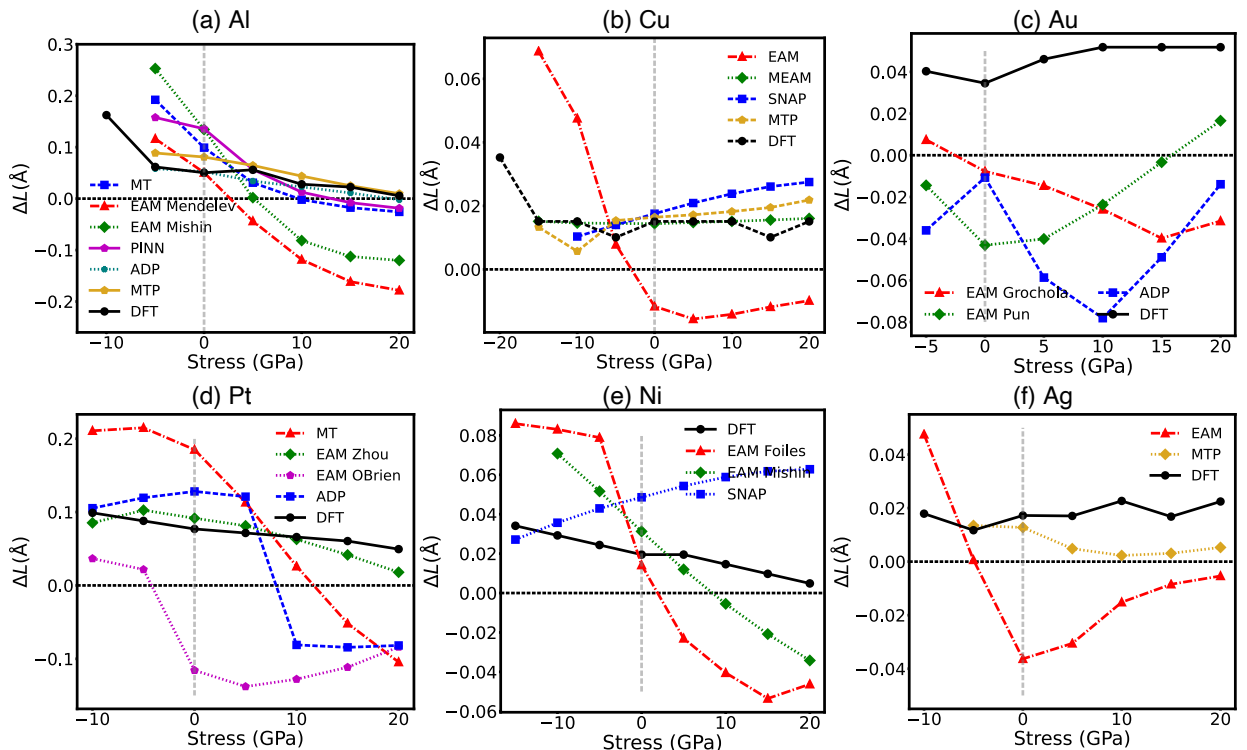


Figure 11: SF formation volume as a function of normal stress obtained by DFT calculations and with interatomic potentials. (a) Al, (b) Cu, (c) Au, (d) Pt, (e) Ni, and (f) Ag. The vertical dashed line corresponds to zero stress and serves as a visual guide.

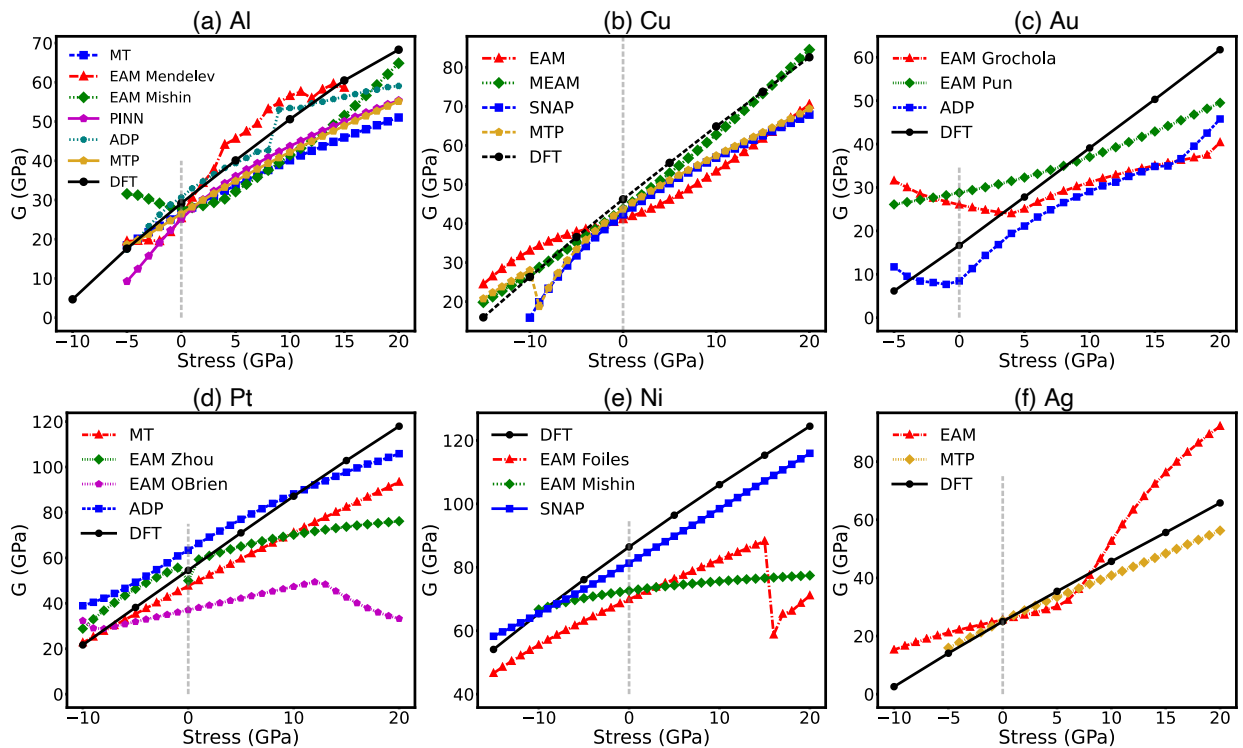


Figure 12: The shear modulus on the  $\{111\}$  plane along the  $\langle 112 \rangle$  direction obtained by DFT calculations and with different interatomic potentials. (a) Al, (b) Cu, (c) Au, (d) Pt, (e) Ni, and (f) Ag. The vertical dashed line corresponds to zero stress and serves as a visual guide.

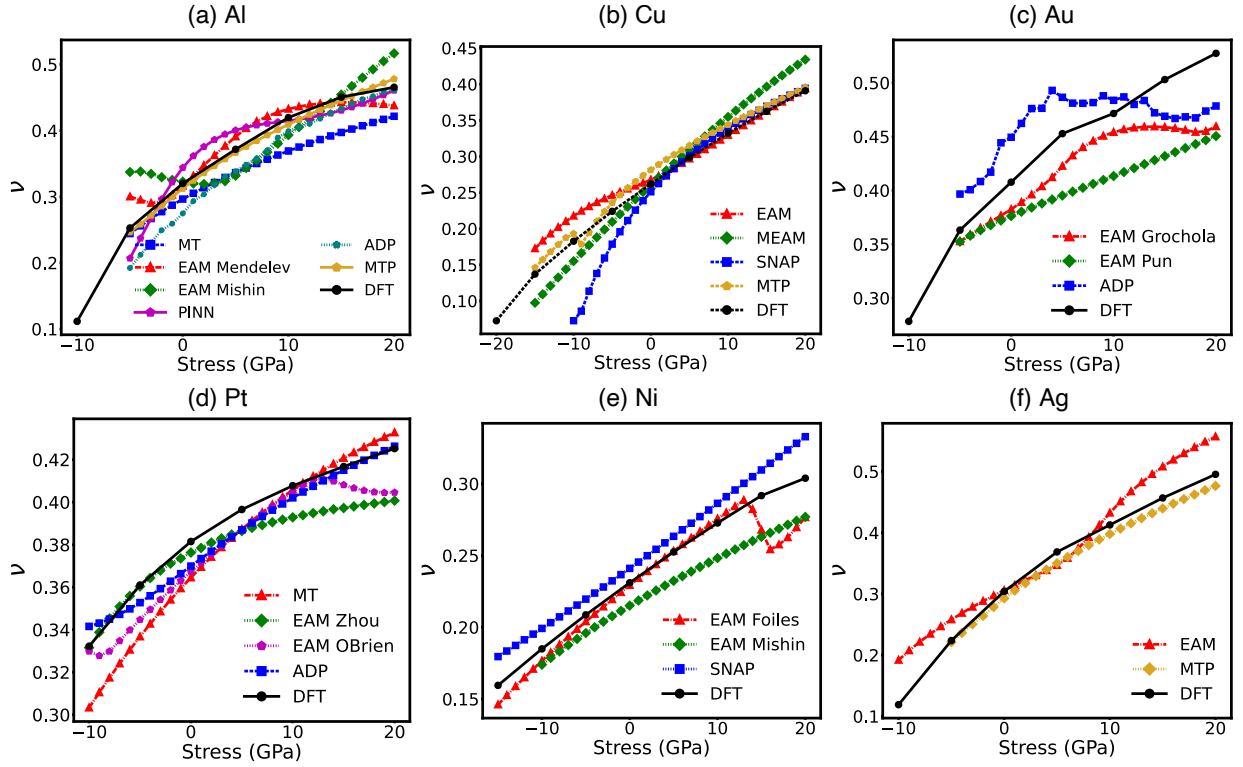


Figure 13: Poisson's ratio obtained by DFT calculations and with interatomic potentials. (a) Al, (b) Cu, (c) Au, (d) Pt, (e) Ni, and (f) Ag.

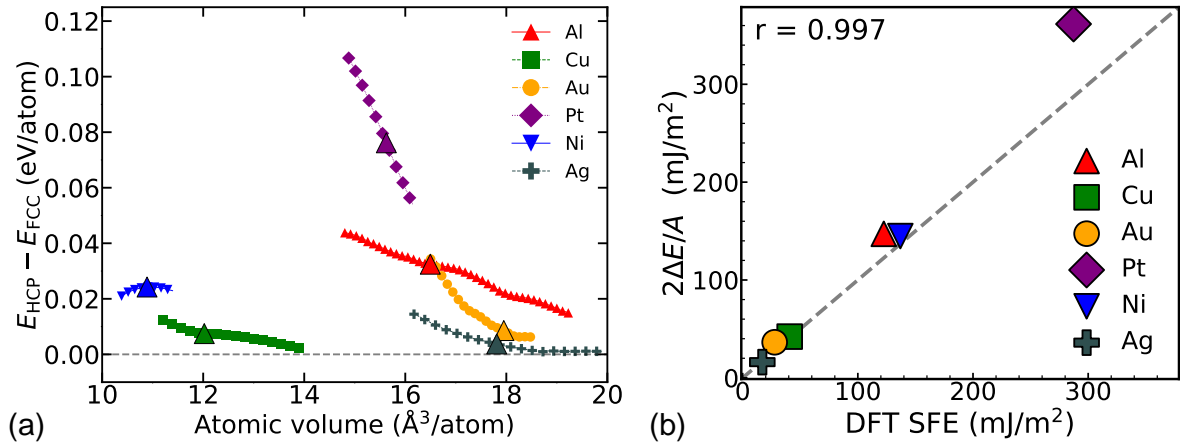


Figure 14: (a) HCP-FCC energy difference for six FCC metals obtained by DFT calculations as a function of atomic volume. Only the atomic volumes for which the SF energy remains stable are included. The triangular symbols mark the data for the equilibrium FCC volume. (b) Comparison the SFE with predictions of Eq.(3). The dashed line represents perfect agreement.

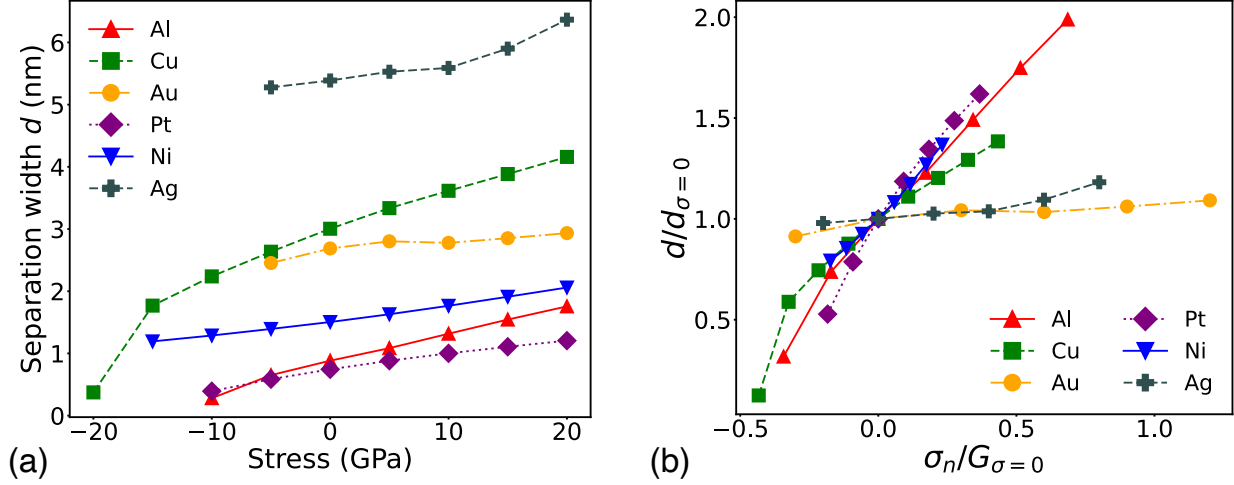


Figure 15: Dissociation width of an edge dislocation as a function of normal stress in six FCC metals obtained from Eq.(4) with input from DFT calculations. (a) Physical coordinates. (b) Normalized coordinates.

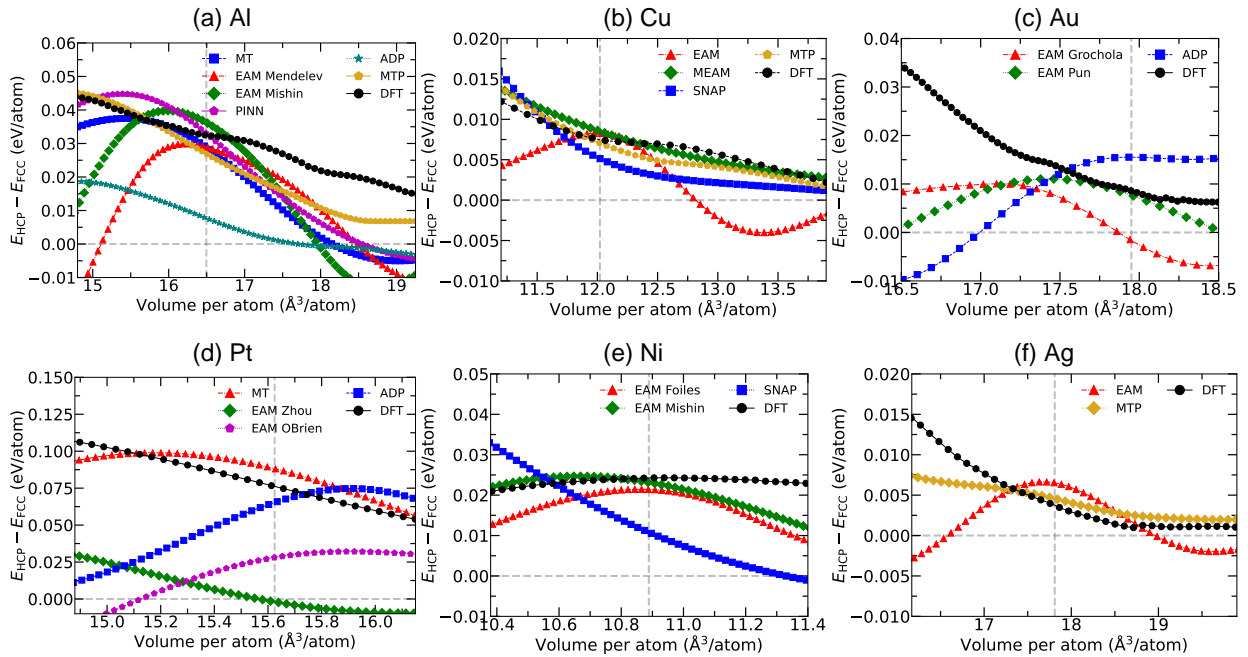


Figure 16: HCP-FCC energy difference for six metals as a function of atomic volume obtained by DFT calculations in comparison with interatomic potentials. Only the atomic volumes for which the SF energy remains stable are included. (a) Al, (b) Cu, (c) Au, (d) Pt, (e) Ni, and (f) Ag. The vertical dashed line corresponds to zero stress and serves as a visual guide.

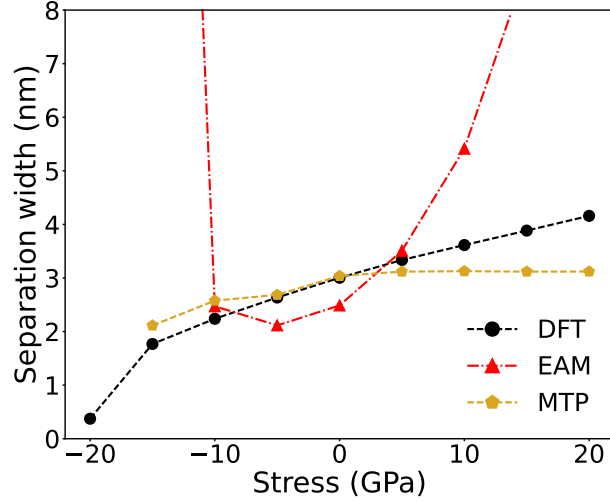


Figure 17: Equilibrium separation between partial dislocations in Cu as a function of applied stresses predicted by Eq.(4) with input from DFT calculations and from the MTP [49] and EAM [52] potentials.

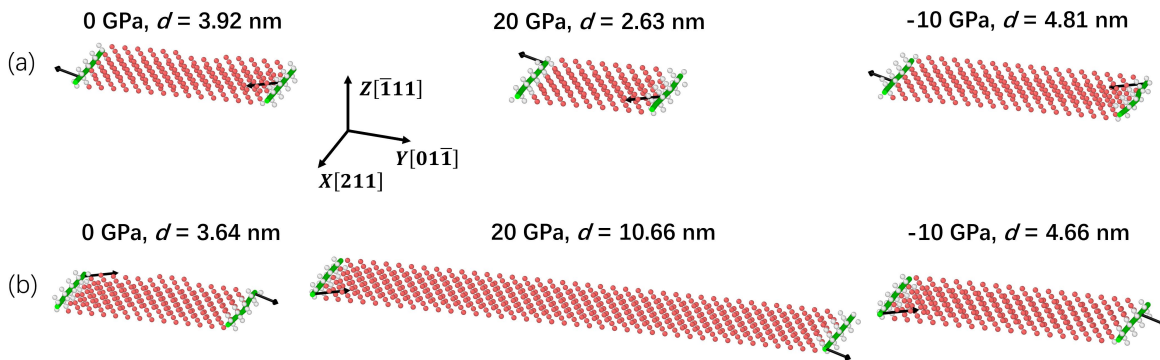


Figure 18: Equilibrium separation distance  $d$  of partial dislocations in Cu subjected to normal stresses of 0, 20, and  $-10$  GPa (positive values indicate compression, negative values indicate tension). (a) Results obtained with the MTP potential [49]. (b) Results obtained with the EAM potential [52]. Green lines mark partial dislocations, and black arrows indicate the Burgers vectors. Atoms within the stacking fault are shown in red. Atoms surrounding the dislocations shown in grey do not belong to any crystalline structure.

Table 1: Interatomic potentials tested in this work.

Label	Potential model	Cite	Fitting/Training data
Al			
MT	Modified Tersoff potential	This work	DFT
EAM Mendelev	Embedded atom method	[53]	DFT + Experiment
EAM Mishin	Embedded atom method	[54]	DFT + Experiment
PINN	Physically-informed neural network	[47]	DFT
ADP	Angular-dependent potential	[55]	DFT
MTP	Moment Tensor potential	This work	DFT
Cu			
EAM	Embedded atom method	[52]	DFT + Experiment
MEAM	Modified embedded-atom method	[56]	Experiment
SNAP	Spectral neighbor analysis potential	[48]	DFT + ab initio MD
MTP	Moment Tensor potential	[49]	DFT
Au			
EAM Grochola	Embedded atom method	[57]	DFT + Experiment
EAM Pun	Embedded atom method	[58]	DFT
ADP	Angular-dependent potential	[55]	DFT
Pt			
MT	Modified Tersoff potential	[44]	DFT
EAM Zhou	Embedded atom method	[59]	Experiment
EAM O'Brien	Embedded atom method	[60]	DFT
ADP	Angular-dependent potential	[44]	DFT
Ni			
EAM Foiles	Embedded atom method	[41, 61]	Experiment
EAM Mishin	Embedded atom method	[62]	DFT + Experiment
SNAP	Spectral neighbor analysis potential	[63]	DFT
Ag			
EAM	Embedded atom method	[64]	DFT + Experiment
MTP	Moment Tensor potential	[49]	DFT

# SUPPLEMENTARY INFORMATION

## The effect of normal stress on stacking fault energy in face-centered cubic metals

Yang Li and Yuri Mishin

Department of Physics and Astronomy, MSN 3F3,  
George Mason University, Fairfax, VA 22030, USA

### A Summary of DFT results

The tables below summarize the main results of the DFT calculations performed in this work. The dash symbol represents cases when the simulation cell was unstable at the applied stress.

Table S1: DFT SF energy (mJ/m<sup>2</sup>) at different normal stresses applied to the fault plane.

	-20 GPa	-15 GPa	-10 GPa	-5 GPa	0	5 GPa	10 GPa	15 GPa	20 GPa
Al	-	-	43.21	88.67	122.52	151.70	174.24	189.96	195.13
Cu	7.59	19.37	27.20	34.42	40.82	47.27	54.29	60.96	67.54
Au	-	-	-	10.26	27.78	49.02	72.59	97.94	124.08
Pt	-	-	196.19	245.27	287.30	325.43	360.47	392.17	420.61
Ni	-	95.69	111.82	125.22	136.89	146.48	154.19	160.44	164.37
Ag	-	-	0.62	8.48	17.04	26.63	37.24	47.29	56.68

Table S2: DFT USFE (mJ/m<sup>2</sup>) at different normal stresses applied to the fault plane.

l	-20 GPa	-15 GPa	-10 GPa	-5 GPa	0	5 GPa	10 GPa	15 GPa	20 GPa
Al	-	-	44.54	106.80	161.10	210.45	255.05	296.68	327.99
Cu	32.68	72.87	105.04	135.58	165.62	195.16	226.02	256.48	287.59
Au	-	-	-	35.59	81.02	131.23	182.85	236.91	292.41
Pt	-	-	207.31	253.79	301.09	348.81	397.66	444.55	491.98
Ni	-	191.24	224.24	255.01	284.81	313.60	341.38	367.95	393.23
Ag	-	-	21.29	60.55	97.39	137.51	177.35	217.80	258.39

Table S3: DFT shear modulus (GPa) corresponding to shear parallel to  $\{111\}$  plane along a  $\langle 112 \rangle$  direction at different normal stresses applied in the  $[111]$  direction.

	-20 GPa	-15 GPa	-10 GPa	-5 GPa	0	5 GPa	10 GPa	15 GPa	20 GPa
Al	-	-	4.68	17.60	29.16	40.09	50.59	60.47	68.30
Cu	1.46	15.96	26.31	36.52	46.20	55.54	64.87	73.74	82.58
Au	-	-	-	6.15	16.66	27.79	39.10	50.30	61.74
Pt	-	-	21.66	38.17	54.52	71.01	87.14	102.84	117.95
Ni	-	54.10	65.39	76.09	86.42	96.42	106.06	115.33	124.48
Ag	-	-	2.58	14.08	25.00	35.38	45.68	55.62	65.79

Table S4: DFT Poisson's ratio (average of  $\nu_{31}$  and  $\nu_{32}$ ) at different normal stresses applied in the  $[111]$  direction.  $\nu_{31}$  and  $\nu_{32}$  correspond to uniaxial strain along  $[111]$  and the transverse strains along  $[1\bar{1}0]$  and  $[11\bar{2}]$ , respectively.

	-20 GPa	-15 GPa	-10 GPa	-5 GPa	0	5 GPa	10 GPa	15 GPa	20 GPa
Al	-	-	0.110	0.248	0.319	0.376	0.417	0.450	0.468
Cu	0.074	0.137	0.184	0.226	0.263	0.299	0.332	0.364	0.394
Au	-	-	-	0.362	0.413	0.451	0.475	0.504	0.524
Pt	-	-	0.332	0.361	0.381	0.396	0.408	0.417	0.425
Ni	-	0.159	0.184	0.208	0.230	0.252	0.272	0.291	0.304
Ag	-	-	0.120	0.225	0.303	0.366	0.418	0.456	0.488

## B The moment tensor potential for Al

In this section, we describe the development of a moment tensor potential (MTP) for Al. The MTP is a machine-learning interatomic potential built on a set of local moment tensor descriptors. For each atom  $i$ , its neighborhood (within a cutoff range) is encoded by the moment tensors [65, 66]

$$\mathbf{M}_{\mu,\nu}(i) = \sum_{j \in \mathcal{N}_i} f_\mu(r_{ij}) \underbrace{\mathbf{r}_{ij} \otimes \cdots \otimes \mathbf{r}_{ij}}_{\nu \text{ times}},$$

where  $\mathbf{r}_{ij}$  is the relative position vector of a neighboring atom  $j$ ,  $r_{ij} = |\mathbf{r}_{ij}|$ ,  $f_\mu(r)$  are radial basis functions, and  $\mu, \nu$  index radial and angular orders, respectively. Scalar basis functions  $B_\alpha(i)$  are then formed as all possible contractions of the moment tensors. These functions are invariant under translations, rotations, and permutations of chemical species. The atomic energy  $E_i$  is expressed as a linear expansion in the basis functions,

$$E_i = \sum_{\alpha} c_{\alpha} B_{\alpha}(i),$$

where  $\{c_{\alpha}\}$  are trainable coefficients. The total energy is then obtained by

$$E_{\text{tot}} = \sum_i E_i.$$

Increasing the maximum tensor orders  $(\mu, \nu)$  expands the basis and raises the effective body order. Training consists of determining  $\{c_\alpha\}$  by minimizing a regularized loss function that interpolates the DFT reference dataset. Further details of MTP training can be found in Refs. [65, 66].

The reference database was composed of energies, forces, and stresses for a set of atomic configurations computed within the density-functional theory (DFT). Calculations were performed with the Vienna *ab initio* Simulation Package (VASP) [35, 36], employing the projector-augmented-wave (PAW) method [37] and the Perdew–Burke–Ernzerhof (PBE) generalized-gradient approximation for exchange-correlation [38]. The PAW dataset used was PAW\_PBE Al (04Jan2001). A plane-wave energy cutoff of 500 eV was applied. Brillouin-zone integrations used Monkhorst–Pack meshes corresponding to a  $\mathbf{k}$ -point density of 10,000  $\mathbf{k}$ -points per reciprocal atom ( $k_{\text{ppa}} = 10,000$ ). First-order Methfessel–Paxton smearing with a width of 0.20 eV was employed, and electronic self-consistency was converged to  $10^{-6}$  eV.

Table S5: DFT database used to create the MTP potential for Al. The first column lists the structure type; the second gives the number of atoms per structure; the third describes the number of configurations for each type of structure.

Structure	Number of atoms	Number of configurations
Bulk deformations, FCC	32	202
Bulk shear deformations, FCC	32	33
AIMD, FCC	32	80
Bulk deformations, A15	8	99
Bulk deformations, BCC	2	120
Bulk deformations, DC	8	109
Bulk deformations,	32	202
Bulk deformations, HEX	1	107
Bulk deformations, SC	8	119
Surface{100}	144	37
Surface{110}	128	40
Surface{111}	16	40
Stacking fault{111}⟨112⟩	30	40
Dimer	2	10
Interstitial	33	50
Vacancy	31, 255	120
Liquid phase	108	51

The DFT database comprised multiple crystalline phases: face-centered cubic (FCC), body-centered cubic (BCC), hexagonal close-packed (HCP), simple cubic (SC), simple hexagonal (HEX), A15, and diamond cubic (DC), as well as liquid, point defects, stacking faults, and free-surface structures. Details of these structures are summarized in Table S5. Bulk structures were subjected to isotropic (volumetric) deformations to generate multiple configurations. In addition, FCC bulk structures were deformed under applied shear and were also relaxed at 500 K using *ab initio* molecular dynamics (AIMD) simulations to generate additional configurations. Free-surface and point-defect models were randomized by applying small atomic displacements to sample distinct local environments. Stacking-fault

(SF) configurations were constructed by imposing shear displacements along  $\langle 112 \rangle$  within the  $\{111\}$  plane. Dimer configurations were generated with varying separation distances. Liquid-phase Al configurations were obtained from molecular dynamics trajectories generated with the EAM Mishin potential [54]. Representative snapshots were subsequently re-evaluated using DFT to obtain energies, forces, and stresses. The volumetrically deformed FCC and HCP bulk structures were assigned more configurations. This choice reflects our observation that the stacking-fault energy (SFE) under normal stress is highly sensitive to the FCC–HCP energy difference as a function of volumetric strain. Emphasizing FCC and HCP configurations at different deformation states improves the MTP’s ability to reproduce the DFT-computed SFE at high stresses.

For liquid-phase configurations, we applied a uniform energy shift of +0.02 eV/atom. This correction is motivated by the tendency of GGA-based DFT to under-predict the melting temperature of Al at low pressure [67]. This trend was confirmed by our own MTP simulations, which yields a melting temperature that was too low. Raising the liquid energies relative to the solid enlarges the solid–liquid free-energy gap and brings the predicted melting temperature closer to experiment. The value of 0.02 eV/atom was selected empirically after testing several shifts and choosing the one that yielded the best melting temperature.

Table S6: Comparison of Al properties from DFT, MTP, MT, PINN [47], EAM [54], and ADP [55] potentials. The properties marked with an asterisk were calculated in this work and are different from those reported in the original publication.

Property	DFT	MTP <sup>†</sup>	MT <sup>†</sup>	PINN	EAM	ADP
$E_0$ (eV/atom)	3.7480 <sup>a</sup>	3.3555	3.3560	3.3604	3.3600	3.3810
$a_0$ (Å)	4.039 <sup>a,d</sup> ; 3.9725–4.0676 <sup>c</sup>	4.0405	4.0284	4.0399	4.0500	4.0254
$B$ (GPa)	83 <sup>a</sup> ; 81 <sup>f</sup>	75	83	81	79	63
$C_{11}$ (GPa)	104 <sup>a</sup> ; 103–106 <sup>d</sup>	106	110	112	114	99 <sup>*</sup>
$C_{12}$ (GPa)	73 <sup>a</sup> ; 57–66 <sup>d</sup>	59	70	65	62	46 <sup>*</sup>
$C_{44}$ (GPa)	32 <sup>a</sup> ; 28–33 <sup>d</sup>	32	39	28	32	39 <sup>*</sup>
$\gamma_S(100)$ (J/m <sup>2</sup> )	0.92 <sup>b</sup>	0.910	0.761	0.904	0.944	0.822
$\gamma_S(110)$ (J/m <sup>2</sup> )	0.98 <sup>b</sup>	0.951	0.818	0.954	1.006	0.858
$\gamma_S(111)$ (J/m <sup>2</sup> )	0.80 <sup>b</sup>	0.802	0.641	0.804	0.871	0.784
$E_v^f$ (eV)	0.6646–1.3458 <sup>c</sup> ; 0.7 <sup>e</sup>	0.694	0.670	0.703	0.676	0.734
$E_v^m$ (eV)	0.3041–0.6251 <sup>c</sup>	0.639	0.575	0.628	0.636	0.649
$E_f^T$ (Td) (eV)	2.2001–3.2941 <sup>c</sup>	3.319	2.837	2.706	3.105	3.177
$E_f^T$ (Oh) (eV)	2.5313–2.9485 <sup>c</sup>	2.833	2.649	2.739	2.798	2.780
$E_f^T <100>$ (eV)	2.2953–2.6073 <sup>c</sup>	2.721	2.342	2.517	2.600	2.575
$E_f^T <110>$ (eV)	2.5432–2.9809 <sup>c</sup>	2.900	2.674	2.843	2.930	2.917
$E_f^T <111>$ (eV)	2.6793–3.1821 <sup>c</sup>	3.232	2.838	2.775	3.018	3.129
$\gamma_{SF}$ (mJ/m <sup>2</sup> )	134 <sup>i</sup> ; 145.67 <sup>g</sup> ; 158 <sup>h</sup> ; 123 <sup>†</sup>	116	134	134	145	40
$\gamma_{US}$ (mJ/m <sup>2</sup> )	162 <sup>j</sup> ; 175 <sup>h</sup> ; 161 <sup>†</sup>	150	163	150	167	135
$T_m$ (K)	933 (Experiment) <sup>k</sup>	966	928	975	1038	855 <sup>*</sup>

<sup>a</sup>Ref [68], <sup>b</sup>Ref[69], <sup>c</sup>Ref[70], <sup>d</sup>Ref [71], <sup>e</sup>Ref[72], <sup>f</sup>Ref[73], <sup>g</sup>Ref[74], <sup>h</sup>Ref[75],

<sup>i</sup>Ref[76], <sup>j</sup>Ref[77], <sup>k</sup>Ref[78]. <sup>†</sup>This work.

The reference dataset was randomly divided into training (70%) and validation (30%) subsets. The training subset was employed to fit the MTP model. Default weights of 1.0, 0.01, and 0.001 were assigned to the energy, forces, and stress components, respectively. The cutoff radius was set to 6.0 Å, with a minimum cutoff of 0.5 Å. Among several cutoff values examined here, this choice provided the most accurate and stable results. An MTP of level 16 was used. Several random training/validation splits were performed, and in all cases the trained MTP accurately reproduced the DFT-calculated energies of the validation configurations. Results for one representative split, comparing DFT-calculated energies with MTP-predicted energies for both the training and validation sets, are shown in Fig. S1. Strong correlation is observed between the DFT-computed and MTP-predicted total energies, confirming that the MTP is well-trained without noticeable under-fitting or over-fitting. The average absolute differences of the MTP and DFT-computed energy per atom are 6.2 meV/atom and 6.8 meV/atom.

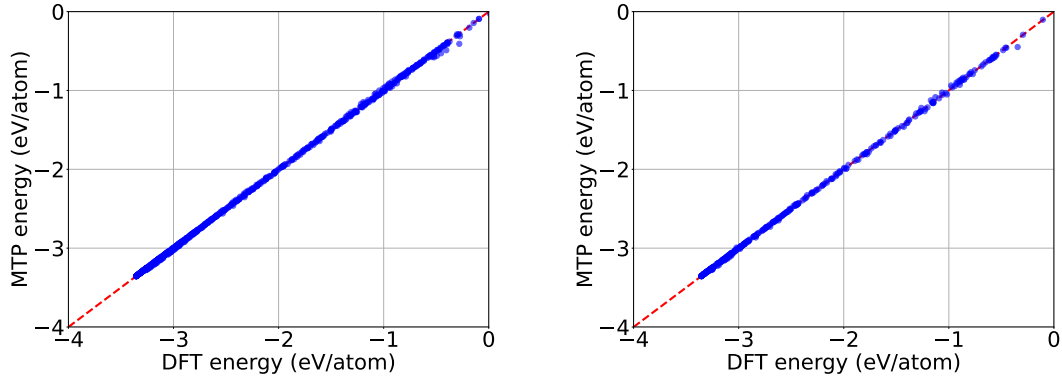


Figure S1: Comparison of DFT-computed and MTP-predicted energies of Al in the training set (left) and the validation set (right). The dashed lines represent that the perfect match.

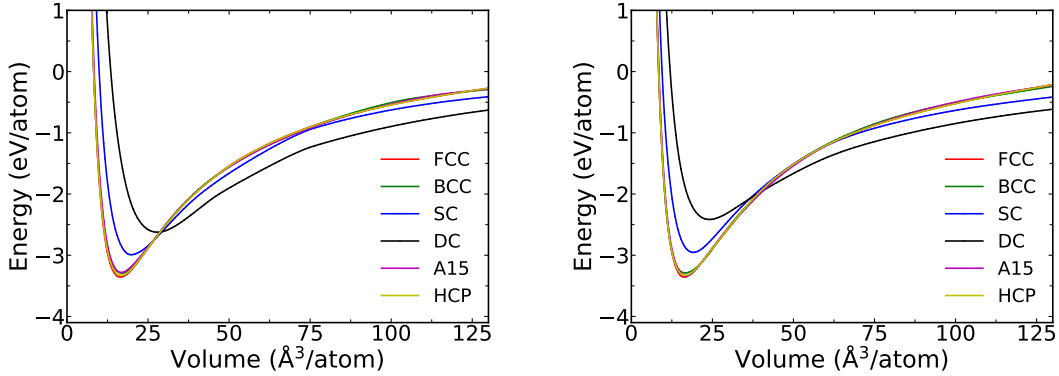


Figure S2: Equation of states of Al computed with the MTP (left) and MT (right) potentials developed in this work.

Since the MTP model employed in this work has a minimum cutoff distance of 0.5 Å, unphysical atomic motions may occur if two atoms approach closer than this limit. To prevent such artifacts, the Ziegler–Biersack–Littmark (ZBL) screened nuclear repulsion potential [84] was applied to describe short-range, high-energy atomic collisions. The cutoff

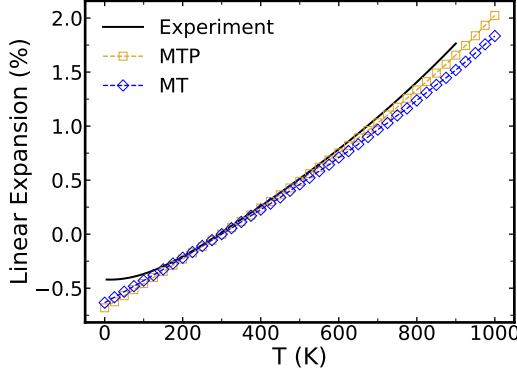


Figure S3: Linear thermal expansion relative to room temperature (293K) predicted by the MTP and MT potentials for Al in comparison with experimental data [79].

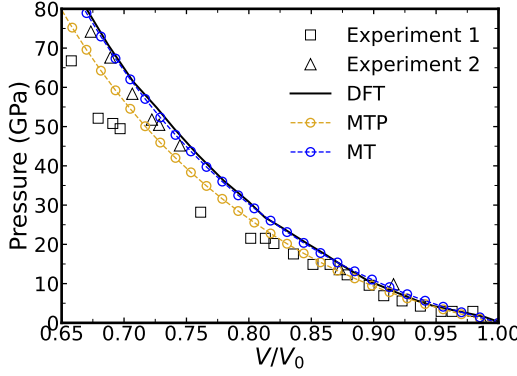


Figure S4: Isotropic compression predicted by the MTP and MT potentials for Al in comparison with DFT calculations [80] and two sets of experimental data (Experiment 1: Ref.[81]; Experiment 2: Ref.[82] ).

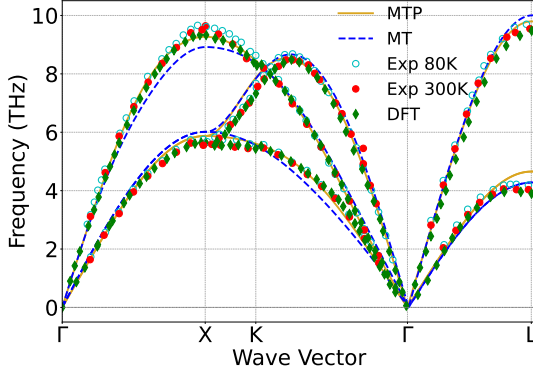


Figure S5: Phonon dispersion curves of Al computed at 0 K with the MTP and MT potentials in comparison with DFT [47] and experimental data [83].

distance for the ZBL interaction was set to 1.0 Å, and the switching function was activated at 0.5 Å. Consequently, whenever two atoms approach within 1.0 Å(a regime where the MTP may lose accuracy due to the absence of such configurations in the training database) the ZBL potential introduces a strong repulsive force, effectively preventing unphysical

atomic overlap.

The Al properties predicted by the MTP potential developed in this work are summarized in Table S6. For comparison, we also include the properties predicted by the DFT calculations, the modified Tersoff (MT) potential developed in this work, the PINN potential [47], the EAM potential [54], and the ADP potential [55]. For the ADP potential, the results for the elastic constants  $C_{11}$ ,  $C_{12}$ ,  $C_{44}$ , and the melting temperature  $T_m$  calculated in this work differ from the values reported in the original publication [55]. All defect energies correspond to fully relaxed configurations. The phonon dispersion curves were computed using the phonopy code [85]. The melting temperature was calculated using the phase coexistence method [86–88]. A periodic simulation cell was first equilibrated in the NPT ensemble at the expected melting temperature and zero pressure. One half of the cell was then heated to form a liquid phase, while the other half remained solid. The entire system was relaxed in the NPH (constant enthalpy) ensemble. During the relaxation, the solid–liquid interface moved as the volume fractions of the solid and liquid phases adjusted the equilibrium. In the process, the system temperature evolved until it converged to a value corresponding to the melting temperature at the ambient pressure.

The performance of the MTP and MT potentials in reproducing the equation of states, thermal expansion, pressure-volume relationship, and phonon dispersion relation, as well as their comparison with DFT and experimental data, are shown in Figs. S2, S3, S4, S5.

## C The modified Tersoff potential for Al

In this section, we describe the development of a new modified Tersoff (MT) potential for Al.

In the MT model, the total energy of a single-component system is represented in the form

$$E = \frac{1}{2} \sum_{i \neq j} V_{ij}(r_{ij}),$$

where  $r_{ij}$  is distance between atoms  $i$  and  $j$ . The pair interaction energy  $V_{ij}$  is represented in the form

$$V_{ij} = f_c(r_{ij}) [A \exp(-\lambda_1 r_{ij}) - b_{ij} B \exp(-\lambda_2 r_{ij}) + c_0], \quad (5)$$

where the bond order factor  $b_{ij}$  is given by

$$b_{ij} = (1 + \xi_{ij}^\eta)^{-\delta}. \quad (6)$$

Here,  $\xi_{ij}$  is an angular-dependent three-body sum

$$\xi_{ij} = \sum_{k \neq i, j} f_c(r_{ik}) g(\theta_{ijk}) \exp [\alpha(r_{ij} - r_{ik})^\beta], \quad (7)$$

where  $\theta_{ijk}$  is the angle between the bonds  $ij$  and  $ik$ . Physically,  $(1 + \xi_{ij})$  represent an effective coordination number of atom  $i$ . The cutoff function  $f_c(r_{ij})$  is has the form

$$f_c(r) = \begin{cases} 1, & r \leq R_1 \\ \frac{1}{2} + \frac{9}{16} \cos \left( \pi \frac{r - R_1}{R_2 - R_1} \right) - \frac{1}{16} \cos \left( 3\pi \frac{r - R_1}{R_2 - R_1} \right), & R_1 < r < R_2 \\ 0, & r \geq R_2, \end{cases}$$

Table S7: Optimized parameters of the MT potential for Al developed in this work.

Parameter	Value		
$A$ eV	$9.410980 \times 10^2$	$c_1$	$3.412730 \times 10^{-1}$
$B$ eV	$1.440410 \times 10^1$	$c_2$	$-4.205600 \times 10^{-1}$
$\lambda_1$ (Å $^{-1}$ )	$2.860720 \times 10^0$	$c_3$	$4.362630 \times 10^0$
$\lambda_2$ (Å $^{-1}$ )	$8.590480 \times 10^{-1}$	$c_4$	$1.032600 \times 10^1$
$\eta$	$5.199240 \times 10^0$	$c_5$	$1.83167 \times 10^0$
$\eta \times \delta$	$5.790380 \times 10^0$	$h$	$2.557150 \times 10^{-1}$
$\alpha$	$1.820040 \times 10^0$	$R_1$ (Å)	$5.633770 \times 10^0$
$\beta$	1	$R_2$ (Å)	$6.588574 \times 10^0$
$c_0$ (eV)	$2.146950 \times 10^{-2}$		

where  $R_1$  and  $R_2$  are the inner and outer cutoff radii. The angular function  $g(\theta_{ijk})$  has the form

$$g(\theta) = c_1 + \frac{c_2(h - \cos \theta)^2}{c_3 + (h - \cos \theta)^2} \left\{ 1 + c_4 \exp[-c_5(h - \cos \theta)^2] \right\}.$$

The original version of this model was proposed by Tersoff [89–91] and modified by Kumagai et al. [45] by generalizing the angular function  $g(\theta)$ . It was recently proposed [46] to add the coefficient  $c_0$  in Eq.(5) for better control of the attractive part of the potential. The potential has 16 free parameters:  $A$ ,  $B$ ,  $\alpha$ ,  $h$ ,  $\eta$ ,  $\lambda_1$ ,  $\lambda_2$ ,  $R_1$ ,  $R_2$ ,  $\delta$ ,  $c_0$ ,  $c_1$ ,  $c_2$ ,  $c_3$ ,  $c_4$  and  $c_5$ . The power  $\beta$  is a fixed odd integer. In this work, we chose  $\beta = 1$ .

For strongly covalent elements, such as Si and C, the outer cutoff  $R_2$  is chosen between the first and second coordination shells of the diamond cubic structure. In this work, we apply the MT model to a metal (Al) by expanding the outer cutoff to 6.56 Å, which includes several coordination shells. In this form, MT becomes a many-body atomic interaction model similar to MEAM and ADP, with  $b_{ij}$  in Eq.(6) playing the role of the embedding function and  $\xi_{ij}$  being similar to the electron density function.

The MT potential was trained on a DFT database similar to that used to train the MTP potential. The optimized parameters are listed in Table S7. The properties predicted by the MT potential are summarized in Table S6 and in Figs. S2, S3, S4, S5. The potential underestimates the surface energies relative to the experimental data and DFT calculations, as do many EAM potentials. The predicted melting temperature of Al is very accurate without fitting. Overall, the potential demonstrates the accuracy on par with some of the best EAM and ADP potentials for metals.

## D Effect of stress on the correlation between stacking fault energy and HCP-FCC energy difference

In the main text, we discussed the correlation between the equilibrium SFE  $\gamma_{\text{SFE}}$  and the HCP-FCC energy difference  $\Delta E$  (per atom). The theoretical prediction of this correlation is expressed by the equation

$$\gamma_{\text{SF}} = 2\Delta E/A, \quad (8)$$

where  $A$  is the area per atom on the (111) plane of the SF. In the main text, we compared the DFT values of  $\gamma_{\text{SFE}}$  with predictions from Eq.(8) in the absence of normal stress. The  $\Delta E$  values appearing in this equation were computed by considering the HCP and FCC phases at the same atomic volume equal to the stress-free atomic volume of the FCC phase. The results were shown in Fig. 14(b) and reveal a significant correlation across the six FCC metals studied in this work. Here, we examine this correlation under applied normal stresses  $\sigma_n$  within the stress interval in which both phases remain mechanically stable.  $\Delta E$  was computed under the constraint that the HCP structure has the same in-plane atomic density in the (111) plane as the FCC structure, and the comparison is made at the same atomic volume. The normal stress is defined as the stress along the [111] direction in the FCC structure. The corresponding stress in the HCP structure is slightly different but remains very close in magnitude. Figure S6 shows the comparison for several representative stresses. The plots show that the correlation persists and not limited to stress-free SFs but persists under both tensile and compressive stresses.

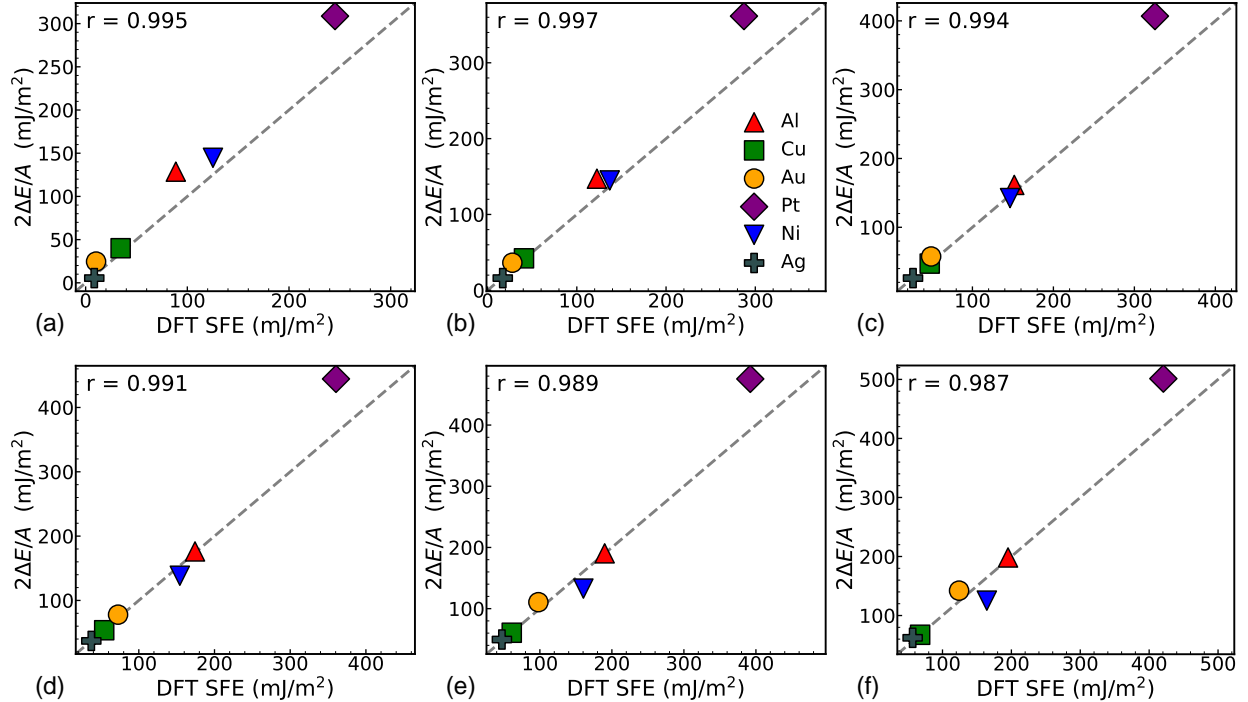


Figure S6: SFE for six metals obtained by DFT calculations and predicted by Eq.(8) using the HCP-FCC energy difference  $\Delta E$ . The dashed line represents perfect agreement between the two calculations. The different panels correspond to the following values of the normal stress  $\sigma_n$ : (a) -5 GPa. (b) 0 GPa. (c) 5 GPa. (d) 10 GPa. (e) 15 GPa. (f) 20 GPa. The strength of correlation is measured by Pearson's correlation factor  $r$  indicated in the top left corner of each plot.

## E Dislocation dissociation width from atomistic simulations

In Section 4.3 of the main text, we presented the results of atomistic simulations of dislocation dissociation into Shockley partials. The simulations were performed for an edge dislocation using the MTP [49] and EAM [52] potentials. The table below summarizes the results for different dimensions of the simulation block to evaluate the size convergence. Although the dissociation width varies with the block size, this dependence does not alter the main conclusions of the main text.

Table S8: Simulation results for the partial dislocation separation width  $d$  in Cu under the normal stresses of 0, 20, and  $-10$  GPa using the MTP [49] and EAM [52] potentials.

Model size (nm <sup>3</sup> )	$d$ at 0 GPa (nm)	$d$ at 20 GPa (nm)	$d$ at $-10$ GPa (nm)
EAM			
$1.8 \times 15 \times 12$	3.25	5.81	3.89
$0.9 \times 15 \times 12$	3.25	5.94	3.89
$0.9 \times 30 \times 25$	3.51	8.88	4.53
$0.9 \times 61 \times 50$	3.64	10.42	4.66
$0.9 \times 122 \times 100$	3.64	10.66	4.66
MTP			
$1.8 \times 15 \times 12$	3.53	2.37	3.79
$0.9 \times 15 \times 12$	3.53	2.37	3.79
$0.9 \times 30 \times 25$	3.91	2.63	4.56
$0.9 \times 61 \times 50$	4.04	2.63	4.82
$0.9 \times 122 \times 100$	3.92	2.63	4.81